DESIGN AND CHARACTERISATION OF AN IMPROVED SPINAL CANAL OCCLUSION TRANSDUCER

by

Bartholomew Scicchitano

B.Sc. The University of Adelaide, 2008

B.Eng. The University of Adelaide, 2012

A THESIS SUBMITTED IN PARTIAL FULFILLMENT OF

THE REQUIREMENTS FOR THE DEGREE OF

MASTER OF APPLIED SCIENCE

in

THE FACULTY OF GRADUATE AND POSTDOCTORAL STUDIES

(Mechanical Engineering)

THE UNIVERSITY OF BRITISH COLUMBIA

(Vancouver)

December 2015

Abstract

The spinal canal occlusion transducer (SCOT) is a sensor used to detect changes in geometry of the cervical spinal canal. A constant current field is created in saline filling the SCOT casing. Radial compression of the SCOT casing results in a change in cross sectional area and an increased resistance to current flow. Sensing elements along the SCOT are used to detect the change in potential difference along the length of the probe and quantify the change in area of the SCOT casing. Shortfalls of the existing SCOT iteration were identified for improvement. These included long term durability and stability of the signal. A new design for the SCOT probe was sought with the aim of addressing these shortfalls.

Six prototype SCOT probes were designed, manufactured and tested. Prototypes considered sensing elements, the casing materials used, input signal conditions and the method used to construct the SCOT probe. Signal to noise ratio and stability of signal were used to compare the prototypes against the original SCOT. The design chosen consisted of a heat shrink casing, 3.97 mm diameter SS ball bearings for ground and excitation elements, and 3.18 mm diameter SS ball bearings for sensing elements. Electrical connections were soldered. A sinusoidal input with frequency of 3 kHz and peak to peak amplitude of 1.5 V was used.

The minimum measurable total canal area was 107.6 ± 1.2 mm^2. The signal to noise ratio of the new SCOT was 74.3 dB and the variation of unoccluded SCOT signal was found to be 1.4 ± 2.5 mV_{RMS} compared to 74.4 dB and 2.3 mV_{RMS} for the previous iteration.

The new SCOT was used in a flexibility study of cervical spine segments. Specimens were loaded in flexion-extension, left-right lateral bending and axial rotation up to 4 Nm at 2 ˚/s. Mean maximum percent decreases in total canal area were 5.8%, 15.9%, 5.1%, 4.6%, 4.6% and 4.2% for flexion, extension, left axial rotation, right axial rotation, left lateral bending, and right lateral bending, respectively. Only extension consistently demonstrated mean maximum decreases that exceeded the mean error of the SCOT (5.3 ± 1.3 mm^2).

Preface

This thesis was written entirely by Bartholomew Scicchitano. Dr. Peter Cripton guided the development of test methodologies and the writing of this thesis. All testing and data analysis presented in Chapters 2 and 3 were performed by Bartholomew Scicchitano. Specimen preparation and testing presented in Chapter 4 was completed with the assistance of Angela Melnyk and Kenneth Martens. All data analysis presented in Chapter 4 was completed by Bartholomew Scicchitano.

The University of British Columbia Human Ethics Board provided ethical approval under the certificate H04-70219 – Biomechanics of Spinal Cord Injury: High Speed Experimental Investigations.

Table of Contents

List of Tables

List of Figures

List of Symbols

V	Potential difference (or Volts)
I	Current
R	Resistance
Δx_k	Length of the k^{th} element
A_k	Cross-sectional area of the k^{th} element
ρ	Resistivity of a fluid
dV_{RMS}	Consistency of unoccluded SCOT
SNR_{dB}	Signal to noise ratio in decibels
μ	Mean of a variable
σ	Standard deviation of a variable
V_{pp}	Peak to peak voltage
V_{RMS}	Root mean square voltage
$f_{poly\ n}$	n^{th} order polynomial

Glossary

AOJ	Atlanto-occipital joint
AAJ	Atlanto-axial joint
CVJ	Craniovertebral junction
FSU	Functional spinal unit
IVD	Intervertebral disc
SCI	Spinal cord injury
MVC	Motor vehicle collision
NASS	National Accident Sampling System
ATD	Anthropometric test device
PMMA	Polymethylmethacrylate
LVDT	Linear variable differential transducer
SCOT	Spinal canal occlusion transducer
TCA	Total cross-sectional area
CT	Computed tomography
SNR	Signal to noise ratio
CCD	Constant current driver
RMS	Root mean square
SS	Stainless steel
SDE	Silver doped epoxy
DAQ	Data acquisition
GOF	Goodness of fit
S_{est}	Standard error of the estimate

ROM	Range of motion
CCS	Central cord syndrome

Acknowledgements

I would like to acknowledge my fellow lab members in the Orthopedic and Injury Biomechanics Group for their continued support throughout my time as a graduate student. I would also like to thank my committee members for reviewing my work and the Canadian Institutes of Health Research for their grant support on this project. Finally, I would like to extend my gratitude to Dr. Peter Cripton for his level headedness, honesty and patience with me as he provided guidance throughout this project.

Beim Menschen ist es wie beim Velo. Nur wenn er faehrt, kann er bequem die Balance halten

Chapter 1: Introduction

Cervical spine injury occurs in 2-3% of all trauma patients [1, 2]. Although rare, injury to the cervical spine is of significance due to the associated high level of morbidity and mortality [2] and the societal and financial impacts on those affected [3-7]. The subaxial cervical spine is the most commonly affected [2]. Injuries to the cervical spine have been investigated previously in regards to the mechanical and structural effects they have on spinal stability [8-11]; however, the possibility of neurological effects is not necessarily a direct translation from changes in structural stability [12].

The spinal canal occlusion transducer (SCOT) is an electromechanical transducer developed as a means of evaluating risk of SCI by quantifying the geometry changes of the spinal canal [13]. A modified version of the original SCOT [14] has been used previously in our lab in a study investigating the effects of lateral eccentricity on the response of cervical spine segments to axial compression loading; however, this sensor suffered from loss of signal, high levels of noise and damage due to corrosion [15]. The rebuild of the SCOT sensor for continued use in the lateral eccentricity study provided the opportunity to include modifications to the design with the aim of improving durability, corrosion resistance and signal properties.

The following thesis describes the design, characterisation and then use of a modified SCOT in a flexibility study to investigate any changes in cervical spinal canal geometry during non-injurious bending.

1.1 Cervical Spine Anatomy

An understanding of the mechanisms of lower cervical spine injury, and the techniques available to measure such injuries, requires an understanding of the anatomy of the lower cervical spine. The following section provides an introduction to the relevant cervical spine anatomy and the anatomical terms used to describe them.

1.1.1 Anatomical Orientation

Anatomical features and movements are described with respect to the three anatomical planes, sagittal, axial, and coronal (Figure 1-1). The sagittal plane is the vertical plane that separates the body into left and right halves. The vertical plane that divides the body into front and back (posterior and dorsal) is called the coronal plane. Finally, the horizontal planes that are perpendicular to both the coronal and sagittal planes are called the axial or transverse planes. Other relevant anatomical terms include proximal (nearer the insertion or attachment of a structure), distal (further from the insertion or attachment of a structure), medial (toward the sagittal plane), lateral (away from the sagittal plane), inferior (anatomy toward the soles of the feet) and superior (anatomy toward the head).

Movements of the cervical spine include flexion-extension, left-right axial rotation and left-right lateral bending. Flexion and extension are that movements occur in the sagittal plane and are forward and backward bending, respectively. Left/right axial rotation is rotation about the superior-inferior axis. Left/right lateral bending occurs primarily in the coronal plane and is the movement of ear toward shoulder.

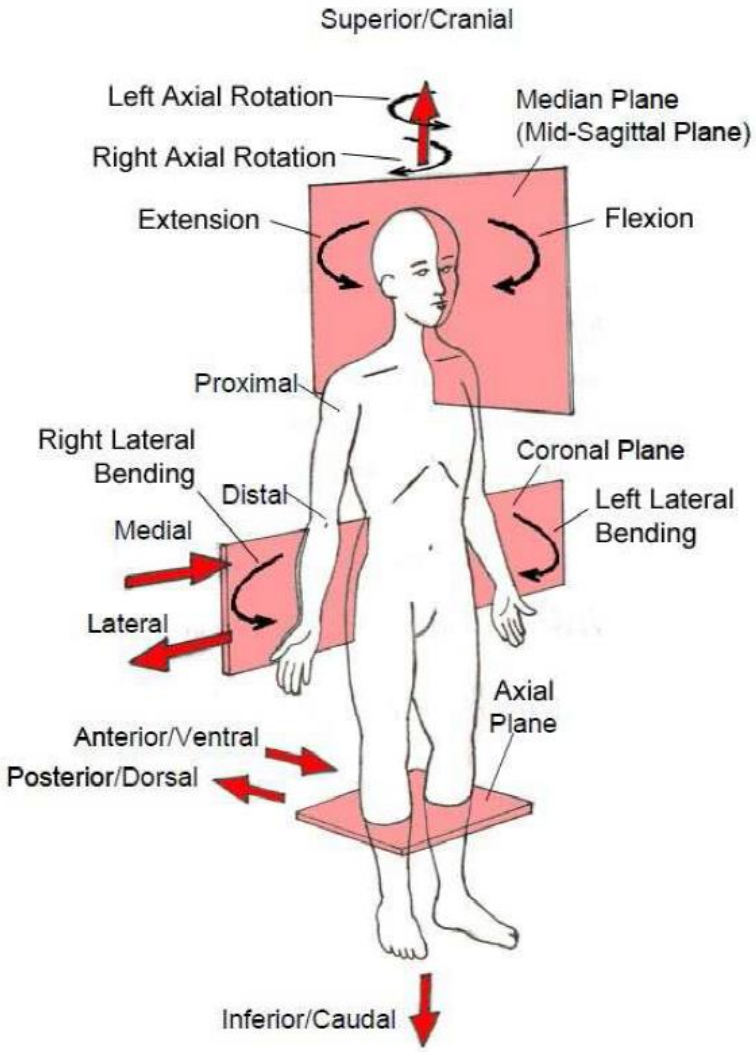

Figure 1-1 Anatomical orientation and terms [15]. Reprinted from Van Toen, C., Biomechanics of cervical spine and spinal cord injury under combined axial compression and lateral bending loading, in Mechanical Engineering. 2013, University of British Columbia: University of British Columbia with permission.

1.1.2 Osteoligamentous Anatomy

The cervical spine consists of seven vertebrae and provides a mobile and stable foundation for the head and protection for the spinal cord. The cervical spine can be described as four functional segments; the atlanto-occipital joint (AOJ), the atlanto-axial joint (AAJ), the joint between the

second cervical vertebra (C2, axis) and the third cervical vertebra (C3) and the lower cervical spine. These functional segments demonstrate unique anatomy that directly influences the stability and mobility of the cervical spine. Since only cervical spine segments below the C2 vertebra (subaxial spine) have been tested in this thesis, a more detailed review of the anatomy of the cervical spine from C2 to the seventh cervical vertebra (C7) is warranted

The C2-C3 joint is typically considered the beginning of the subaxial cervical spine; however, it is often described separately from the lower cervical spine (C3-C7), due to fundamental differences regarding the skeletal anatomy of the C2-C3 facet joints [16]. These differences are best illustrated when viewing the C2-C3 functional spinal unit (FSU) in the plane of the facet joints (pillar view, Figure 1-3). It is evident in the pillar view that the C3 superior articular facets are angled upward and medially, forming a socket in which the inferior articular facets of the C2 sit [16]. Though not fully investigated, Moriya *et al* [17] observed coupled lateral flexion of the C2-C3 joint in the opposite direction to that observed in the lower cervical spine during axial rotation. That is, the unique anatomy of the C2-C3 facet joints elucidate a bending of the C2 vertebra away from the side of rotation.

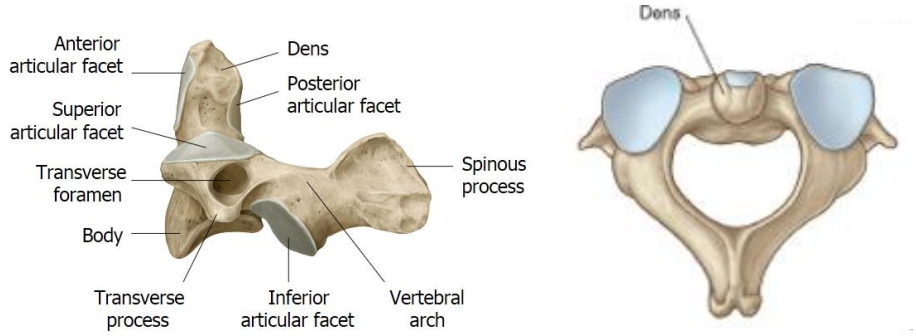

Figure 1-2 Left lateral view (left) [18] and superior view (right) [19] of a typical C2 vertebra. Reprinted from Gilroy, A.M., et al., Atlas of anatomy. 2nd ed. 2012, Stuttgart ; New York: Thieme. xv, 694 p with permission

from Thieme (left). Reprinted from Drake, R.L., et al., Gray's anatomy for students. 2nd ed. 2010, Philadelphia, PA: Churchill Livingstone/Elsevier. xxv, 1103 p with permission from Elsevier (right).

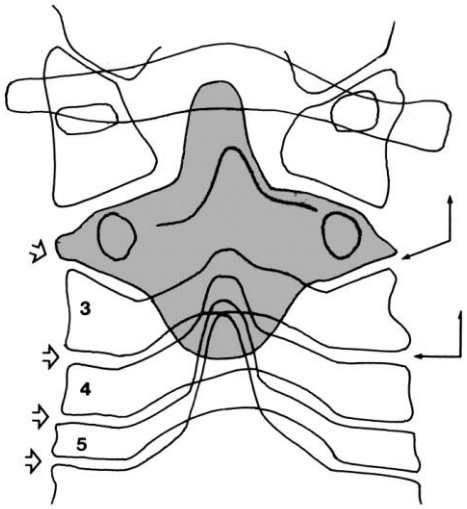

Figure 1-3 Pillar view of the C2 (shaded)-C3 joint. The pillar view highlights the transverse nature of the inferior joints when compared to the C2-C3 facet joint [16]. Reprinted from Bogduk, N. and S. Mercer, Biomechanics of the cervical spine. I: Normal kinematics. Clinical Biomechanics, 2000. 15(9): p. 633-648.16 with permission from Elsevier.

The vertebrae from C3-C7 are the building blocks of the subaxial cervical spine. Each pair of adjacent vertebrae form a FSU consisting of an intervertebral disc (IVD) separating adjacent vertebral bodies, uncovertebral and facet joints. A typical vertebra of the lower cervical spine is presented in Figure 1-4. The vertebral arch and posterior boundary of the vertebral body form the vertebral foramen (spinal canal), which hosts the spinal cord and meninges.

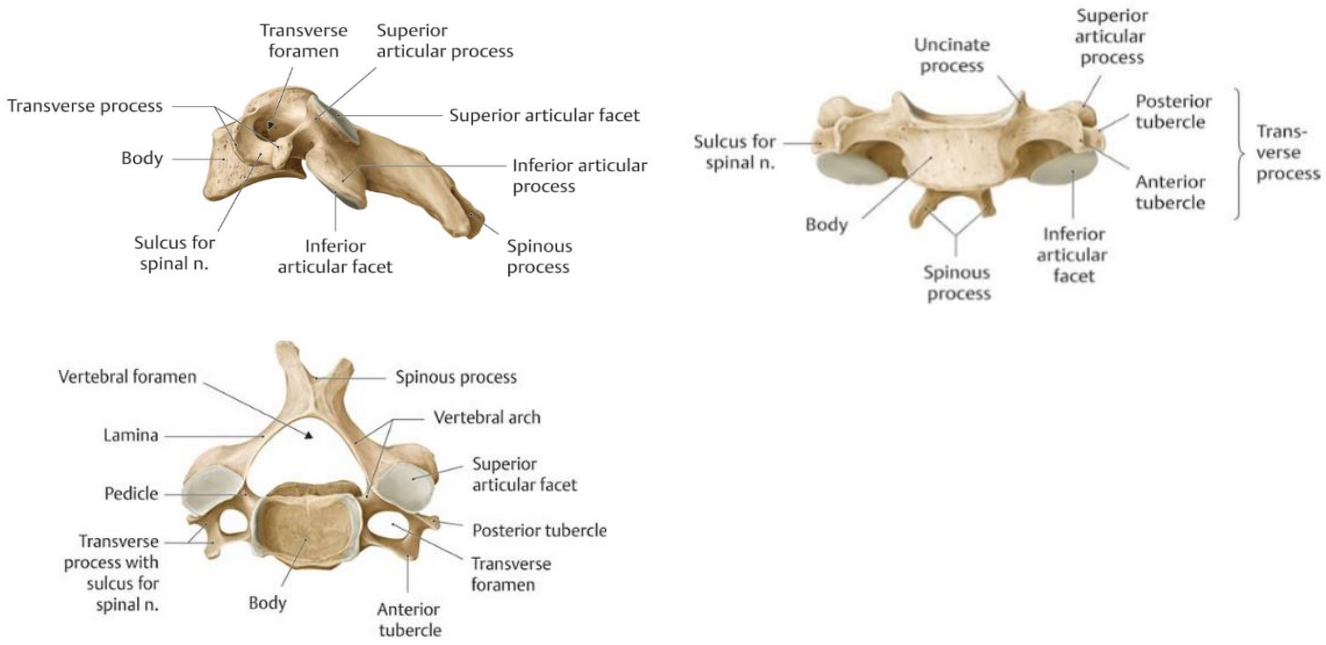

Figure 1-4 Left lateral (top left), anterior (top right) and superior (bottom left) views of a typical vertebra of the lower cervical spine (C4) [18]. Reprinted from Gilroy, A.M., et al., Atlas of anatomy. 2nd ed. 2012, Stuttgart ; New York: Thieme. xv, 694 p with permission from Thieme.

The soft tissue anatomy of the lower cervical spine has a significant contribution to both its stability and mobility. Of particular interest are the IVDs, the joint capsules of the facet joints, the ligamentum flavum and the posterior longitudinal, anterior longitudinal, interspinous and superspinous ligaments (Figure 1-5). The ligamentous structures of the lower cervical spine and the disc are responsible for restriction of movement. The anterior longitudinal ligament, a fibrous band connecting the anterior aspects of vertebral bodies and IVDs. Together with the annulus fibrosis of IVDs, the anterior longitudinal ligament acts to limit extension of the spine. The posterior longitudinal ligament runs along the posterior boundary of the vertebral bodies, inside the spinal canal. The ligamentum flavum and interspinous ligaments connect adjacent vertebrae

posteriorly at the laminae and from root to apex of adjacent spinous processes, respectively. Similarly, the superspinous ligament connects adjacent vertebrae at the apices of the spinous processes, eventually merging superiorly with the nuchal ligament. The joint capsule surrounding the synovial facet joints consists of capsular ligaments extending to just beyond the articular facet of the adjacent vertebra. The facet joints are planar joints with two-dimensional motion in the plane of the facets limited by the joint capsules. Ultimately, the posterior longitudinal ligament, ligamentum flavum, capsules of the facet joints, interspinous and superspinous ligaments work in unison to restrict flexion of the cervical spine.

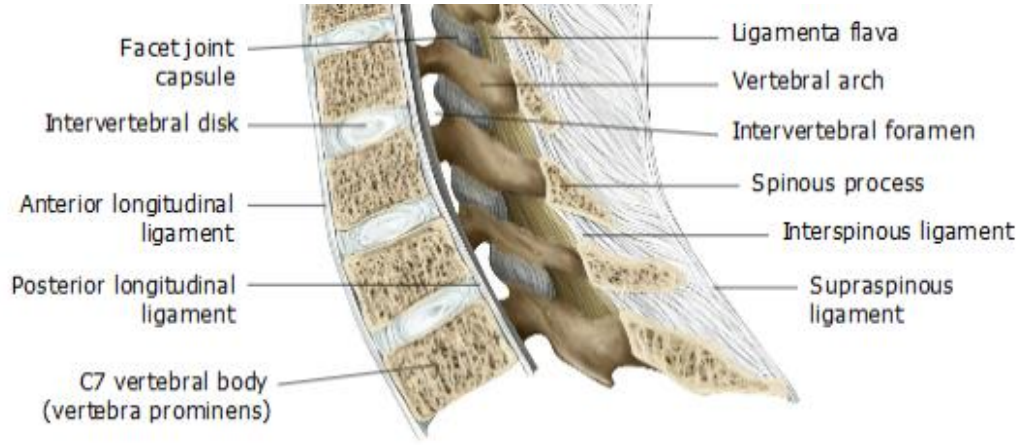

Figure 1-5 Soft tissue anatomy of the lower cervical spine [18]. Reprinted from Gilroy, A.M., et al., Atlas of anatomy. 2nd ed. 2012, Stuttgart ; New York: Thieme. xv, 694 p with permission from Thieme.

1.1.3 Neural Anatomy

The spinal cord allows communication of signals between the brain and the rest of the body (in both directions) and together, the brain and spinal cord form the central nervous system. Damage to the spinal cord can cause a number of pathologies, including paralysis when the signal transmission is inhibited.

The spinal cord is contained within the spinal canal, and is afforded protection by the canal itself, as well as cerebrospinal fluid, and three meningeal membranes.

The two main constituents of neural tissue in the spinal cord are neurons and neuralgia. Neurons consist of a cell body, a dendrite to carry signals to the cell body, and an axon to carry signals away from the cell body, while neuralgia provide support for neurons. The central, 'H' shaped region of the spinal cord is the grey matter, consisting primarily of nerve cell bodies arranged in columns longitudinally along the cord. Surrounding the grey matter is the white matter, consisting of nerve cell processes such as dendrites and axons (Figure 1-6).

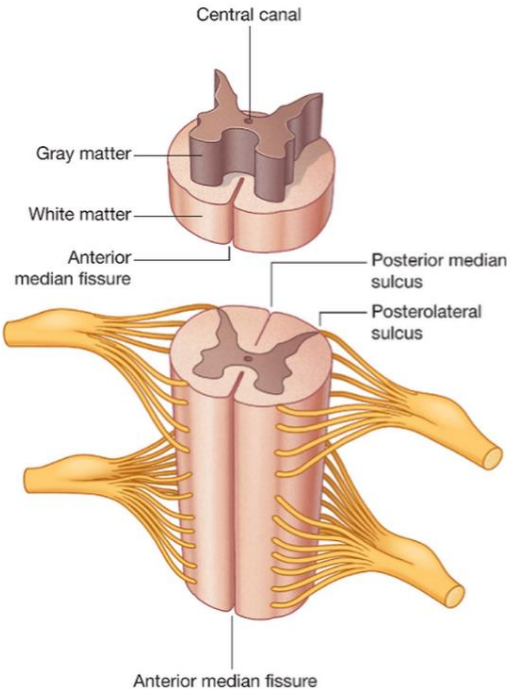

Figure 1-6 Illustration of the spinal cord and its constituents [19] surrounding the spinal cord [19]. Reprinted from Drake, R.L., et al., Gray's anatomy for students. 2nd ed. 2010, Philadelphia, PA: Churchill Livingstone/Elsevier. xxv, 1103 p with permission from Elsevier.

The meningeal membranes protecting the spinal cord are the pia mater, the arachnoid mater, and the dura mater (Figure 1-7) [19]. The pia mater is the innermost meningeal membrane, adhering directly to the spinal cord. The next innermost membrane is the arachnoid mater. The space between the pia mater and the arachnoid mater is the subarachnoid space, and is the region containing the cerebrospinal fluid. Finally, the outermost meningeal membrane is the dura mater.

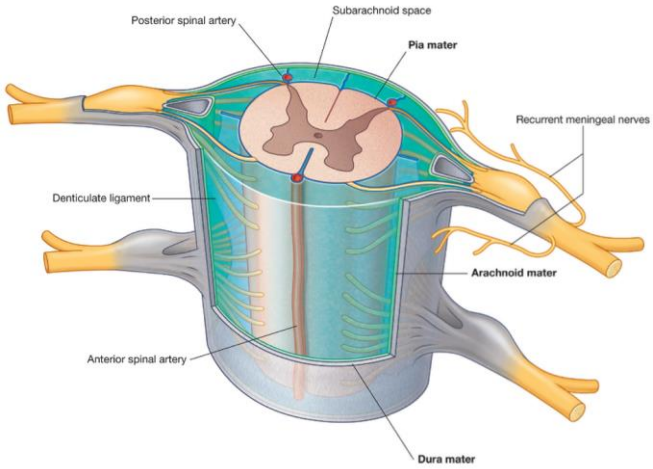

Figure 1-7 Illustration of the meningeal membranes [19]. Reprinted from Drake, R.L., et al., Gray's anatomy for students. 2nd ed. 2010, Philadelphia, PA: Churchill Livingstone/Elsevier. xxv, 1103 p with permission from Elsevier.

1.2 Clinical Problem

1.2.1 Spinal Cord Injury

Spinal cord injury (SCI) can be in the form of complete and incomplete injury. Complete SCI describes a total loss of motor and sensory function below the level of injury. If partial preservation of function below the level of injury occurs, it is described as an incomplete SCI. It has been established that SCI occurs in two phases; the primary phase resulting from the

immediate mechanical insult of the spinal cord, and the secondary phase due to ongoing biochemical changes at the cellular level beyond the time of injury [20]

1.2.2 Epidemiology

The epidemiology of SCI has been studied extensively on a regional, national and international scale (Table 1-1). Incidence of SCI has been reported for provincial Canada as 52.5/million population (total), with 44.3/million population surviving to hospital admission in Alberta [21] and 35.7/million population in British Columbia [22]. Injury at the cervical level is most common [21-25], with males between 3 and 4 times more likely to suffer SCI than females [4, 21, 22, 25-27]. The most common causes for SCI are motor vehicle collisions (MVC), followed by falls, sports related injuries and intentional violence [4, 21-23, 25, 26]. There are no successful treatments or cures for SCI and thus most people who sustain the injury live with the associated paralysis for the remainder of their lives.

The significant societal and financial impacts as a result of SCI have also been reported extensively (Table 1-2). In Canada, the total economic burden of SCI was estimated to be $2.67 billion annually [3]. Estimates for individual lifetime economic burden range from $1.1 million to $4.7 million depending on age at time of injury and level of injury [3, 28]. Societal impacts of SCI include an increased risk of psychological morbidity [6], alcohol and substance abuse [7, 29], suicide [30] and marriage breakdown [5].

Table 1-1 Selection of papers reporting epidemiology of SCI at regional, national and global scales

Author	Region	Focus	Incidence (/million population)	Findings
Dryden *et al* [21]	Alberta, Canada	SCI and cauda equina injury	52.5 (total), 44.3 (survival to hospital admission)	• Rural residence 2.5 times more likely than urban residents • Etiology: MVC (56.4%), falls (19.1%), sports/recreation (11.3%) • Highest MVC incidence between 15 and 29 years; highest falls incidence older than 60 years
Lenehan *et al* [22]	British Columbia, Canada	SCI at single institution between 1994 and 2005	35.7	• Increase in median age over 10 year period (34.5 to 45.5 years) • Etiology: MVC (51.4%), falls (28.5%), sports (17.9%), intentional violence (1.5%) • Highest MVC incidence for age less than 55 years, highest falls incidence older than 55 years • MVC principal cause of male injury (all ages) • Male : Female ratio = 4.4:1
Tator *et al* [24]	Toronto, Canada	Time related changes in acute SCI epidemiology	NA	• Significant increase in sports related SCI between 1947-1973 group and 1974-1981 group • No significant changes in level of injury • Increase in burst fractures between 1947-1973 group and 1974-1981 group
Pickett *et al* [26]	London, Canada	Traumatic SCI at tertiary care centre	42.4 (15-64 years), 51.4 (over 65 years)	• Etiology: MVC (35%), falls (31%), • Male : Female ratio = 3:1
National Spinal Cord Injury Statistical Centre [4, 28]	USA	SCI, nationwide statistics	40	• Etiology: MVC (42.4%), falls (21.8%), violence (17.4%), sports/recreation (10.3%) • Male : Female ratio = 4:1 • Estimated lifetime cost: $4.7 million (C1-C4, age 25), $1.5 million (C5-T1, age 25)

Author	Region	Focus	Incidence (/million population)	Findings
Jackson *et al* [25]	USA	Evaluate epidemiologic trends in SCI	NA	• Male : Female = 4:1 • Mean age was 33 years • Injury at cervical level most common over entire study period • MVC, sports and falls significantly more likely to cause to result in injury at cervical level • Violence more likely to result in injury at thoracolumbar level • Diving most common sport resulting in injury, proportion of injuries from diving is decreasing; proportion of injuries sue to skiing is increasing
Sekhon *et al* [20]	Systematic review, global	Acute SCI	11.5-53.4 (developed countries), 15-40 (global)	• Death after admission range between 4.4 and 16.7% • Younger victims have greater preponderance of injuries in high velocity impacts
Lee *et al* [31]	Global	Traumatic SCI	23 (179312 cases per annum)	

Table 1-2 Selection of papers reporting economic and societal burdens due to SCI

Author	Region	Focus	Findings
Heinemann *et al* [29]	Regional rehabilitation hospital, USA	Substance abuse before and after traumatic SCI	• Recent use (3 or more times in the past 6 months) reported by SCI sample higher than in National Household Survey(1987) in 9 out of 10 substance categories
Tate *et al* [7]	USA	Alcohol and substance abuse among SCI population	• 17% SCI population vs 7.41% general population engaging in at risk drinking behavior • 14.2% SCI population rated as alcohol abusers
Hartkkopp *et al* [30]	Denmark	Relationship between functional status and risk of suicide in SCI population	• Suicide rate 4.6 times higher in SCI population than expected in general population • Between 1972 and 1990, suicide rate was 7.5 times larger in SCI population than expected in general population; 21.8% of suicides identified had gotten their SCI from a previous suicide attempt
Krueger *et al* [3]	Canada	Estimate economic burden of SCI in Canada	• $1.5 million estimated economic burden for incomplete paraplegia • $3 million estimated economic burden for complete tetraplegia • $2.67 billion total economic burden for Canada annually
DeVivo *et al* [5]	USA	Estimate divorce rates for marriages entered into after traumatic SCI	• Higher divorce rate than expected at both 5 and 10 year mark in marriage
Craig *et al* [6]	Systematic review	Review of risk of depression in SCI population	• Rate of significant depressive symptoms in people with SCI living in community 25-30% • People with SCI have higher risk of psychological morbidity than able bodied people

1.3 Quantitative Measurement of Spinal Canal Occlusion

1.3.1 Current State of Research

A number of transducers and surrogate models have been developed as a means of assessing the risk of SCI, based on spinal canal occlusion, in studies of dynamic loading of the spine (Table 1-3). These include the use of pressure transducers[32, 33], displacement sensors [34] and electromechanical transducers [14, 35, 36].

The earliest method of assessing geometric changes of the spinal canal in a cadaveric study of SCI was developed by Chang *et al* [32]. In their study, the spinal cord, dura and nerve roots were removed and replaced with a flexible tube [32]. Water was circulated through the tube during impact loading and the pressure in the fluid monitored upstream to detect changes in canal geometry [32]. The changes in pressure were related to canal area using a two-step calibration method; first, the relationship between tube diameter and fluid pressure was established by monitoring fluid pressure while dial calipers were used to compress the tube [32]. The relationship between tube diameter and cross-sectional area was then calculated by setting polymethylmethacrylate (PMMA) in the tube while the tube was compressed at various depths [32]. The PMMA casts at known compression depths were then sectioned and imaged to calculate cross-sectional area [32]. This work, though novel, was limited by the range of occlusions that could be measured (up to 50%, at which time the fluid flow was cut off) [32], a slow response time to changes in canal geometry and the inability to localize the occlusions identified [34].

Panjabi *et al* developed displacement transducers consisting of a single axis strain gauge bonded to thin steel bent into a leaf spring geometry [34]. The transducers were calibrated quasistatically using a linear variable differential transducer (LVDT), and placed in the spinal canal so that changes in mid sagittal diameter could be monitored [34]. The Panjabi *et al* method was advantageous over that of Chang *et al* [32] due to its localization of occlusion site, faster response time and increased range; however, the transducers were prone to breaking and movement, particularly during impacts that resulted in projectile fracture types, and the quasistatic calibration was not representative of load rates expected in an impact study [34].

The spinal canal occlusion transducer (SCOT) is an electromechanical transducer developed as a means of evaluating risk of SCI by quantifying the geometry changes of the spinal canal [13]. As the SCOT is the focus of this thesis, it will be discussed separately in section 1.3.2.

Surrogate cords have also been used extensively to investigate the risk of SCI during dynamic impact studies, by either visualising the surrogate [37-39], or monitoring it with a transducer [40, 41]. Visualisation of the surrogate cord has been achieved by doping it with a radiopaque substance such as barium sulfate and then imaging the experiments with high speed x-ray (Figure 1-8) [37, 38]. Assessment of SCI risk during impact experiments has also been achieved by marking the surrogate with a grid of enamel dots and removing part of the transverse processes of the spine so that a high speed camera can image it [39]. The requirement to be able to see the cord, either by x-ray or directly, are limiting factors of these methods. Removal of the transverse processes to be able to image the surrogate cord likely influenced the injury mechanics of the spine itself. Though the use of a radiopaque cord allows the specimen to remain intact, this

method has only been used to assess the cord deformations in the sagittal plane and further validation would be required to use it for multi-planar monitoring of the canal.

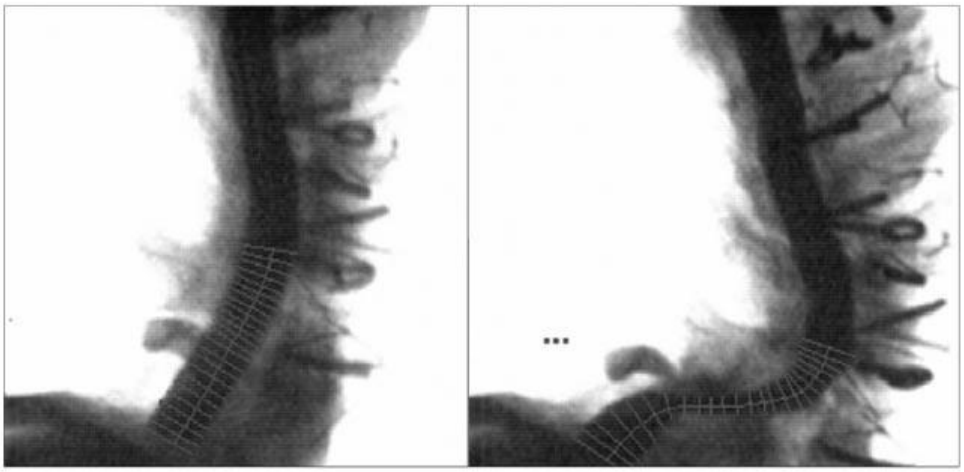

Figure 1-8 Example of barium sulphate doped surrogate cord the spinal cord just prior to (left), and during a head first impact [37]. Reprinted from Saari, A., E. Itshayek, and P.A. Cripton, Cervical spinal cord deformation during simulated head-first impact injuries. Journal of Biomechanics, 2011. 44(14): p. 2565-71 with permission from Elsevier.

Instrumentation of surrogate cords with pressure transducers has also been used previously to assess the risk of SCI [40] and changes in canal geometry [41]. Pintar *et al* monitored the integrity of a surrogate spinal cord during their burst fracture study with embedded thin film pressure transducers [40]. The primary limitation of this work was that the pressure gradients observed were not related to changes in cord area or the risk of neurologic injury [15]. Similarly, Wilcox *et al* used a single catheter tipped pressure transducer embedded in a gelatin surrogate spinal cord during their investigations[41]. Again, no details of how to correlate the changes in pressure with risk of SCI injury or changes in canal geometry were presented, and the use of a

single, axially aligned pressure transducer limited measurements to only a single position in the canal [41].

Geometry changes in the spinal canal have also been quantified by imaging the canal directly with high speed video [42]. Using mirrors above and below the spinal canal, Wilcox *et al* were able to image the canal during impact experiments with their bovine model of burst fractures (Figure 1-9). The total cross-sectional area (TCA) of the canal was then measured digitally frame by frame, and residual occlusions compared with computed tomography images (CT) taken post injury. By imaging the canal directly, Wilcox *et al* demonstrated that in a burst fracture injury, the ultimate level of occlusion (what is imaged by CT in a clinical setting) is less than the maximum occlusion experienced during the event [42]. This occurs because typically, the posterior longitudinal ligament restricts the burst fragment, and pulls it back towards the vertebra from which it came [42]. The result highlights that post injury CT may not be a sufficient indication of potential for neurologic impairment[42]. The requirement for the specimen to be aligned axially, with any natural lordosis removed, may have altered the biomechanics of the specimen during impact and is a limitation of this work[42].

Table 1-3 Methods used to assess risk of SCI in dynamic loading experiments of the spine.

Author	Model	Occlusion Measurement Method	Performance	Notes
Change *et al* (1994) [32]	Cadaver	Upstream pressure measurement of water circulating through canal	• Range=0-54% occlusion • Absolute uncertainty ±5% • 5 ms rise time delay from 14.9 ms impulse	• Two step calibration method • Dynamic calibration required due to pressure wave created in impact scenario
Panjabi *et al* (1995) [34]	Cadaver	Strain gauge bonded to spring steel with feet at ends to allow anchoring at mid sagittal diameter	• Range=6-12 mm • Accuracy=0.106 mm • Maximum observed error of 0.20 mm	• Calibrated quasistatically using LVDT, not representative of dynamic impact environments • Prone to damage and movement • Susceptible to vibration • Improved response time over Chang *et al* [32] method
Pintar *et al* (1996) [40]	Cadaver	7 thin film pressure sensors embedded in surrogate cord	• Sensors validated quasistatically and dynamically within 1%	• Surrogate cord properties validated against *in vivo* feline cord properties
Bilston *et al* (1993) [39]	Physical model	Surrogate cord with enamel dot grid, transverse processes of model vertebrae removed for imaging of grid	NA	• Surrogate cord properties validated against *ex vivo* properties of cadaver spinal cords
Wilcox *et al* (2002) [42]	Bovine	Axially aligned canal positioned between two mirrors, high speed camera imaged canal during experiments	• Error in cross-sectional area approximately 7% • 12% level of agreement between final level of occlusion using CT	• No reliance on calibration of transducers prior to testing • Not affected by superimposed vibrations (cf. Panjabi *et al* [34]) • Non-contact measurement, no restriction of fragments • Full range of canal occlusion measurable • Only suitable for straight spine segments • Cannot localize the occlusion observed • Only validated for post injury measurement of occlusion

Author	Model	Occlusion Measurement Method	Performance	Notes
Kroeker *et al* (2009) [38]	Cadaver	Surrogate cord doped with barium sulphate for imaging with high speed x-ray	• Demonstrated consistent mechanical properties after multiple tests • Linear behavior up to 12% strain	• Surrogate cord tensile properties validated against existing *in vivo* measurements of feline and canine cords • Surrogate cord transverse properties validated against existing *in vivo* measurements of feline cords
Raynak *et al* (1998) [13]	Cadaver	SCOT – electromechanical transducer placed in canal to measure total canal area	• Range=20-100 mm^2 • Resolution=±5 mm^2	• 20 mm length sensing section inhibits exact localization of occlusion • SCOT tube does not fill the spinal canal (outer diameter 15.9 mm), particularly laterally, resulting
Zhu *et al* (2008) [14]	Cadaver	SCOT – based on same design above, but with modified sensing electrode configuration	• Range=40-130 mm^2 * • Resolution=±15 mm^2 * • Accuracy=1.1-13.4 mm^2 *	As above

* Values obtained from unpublished validation study conducted in the current UBC laboratory, August 2013

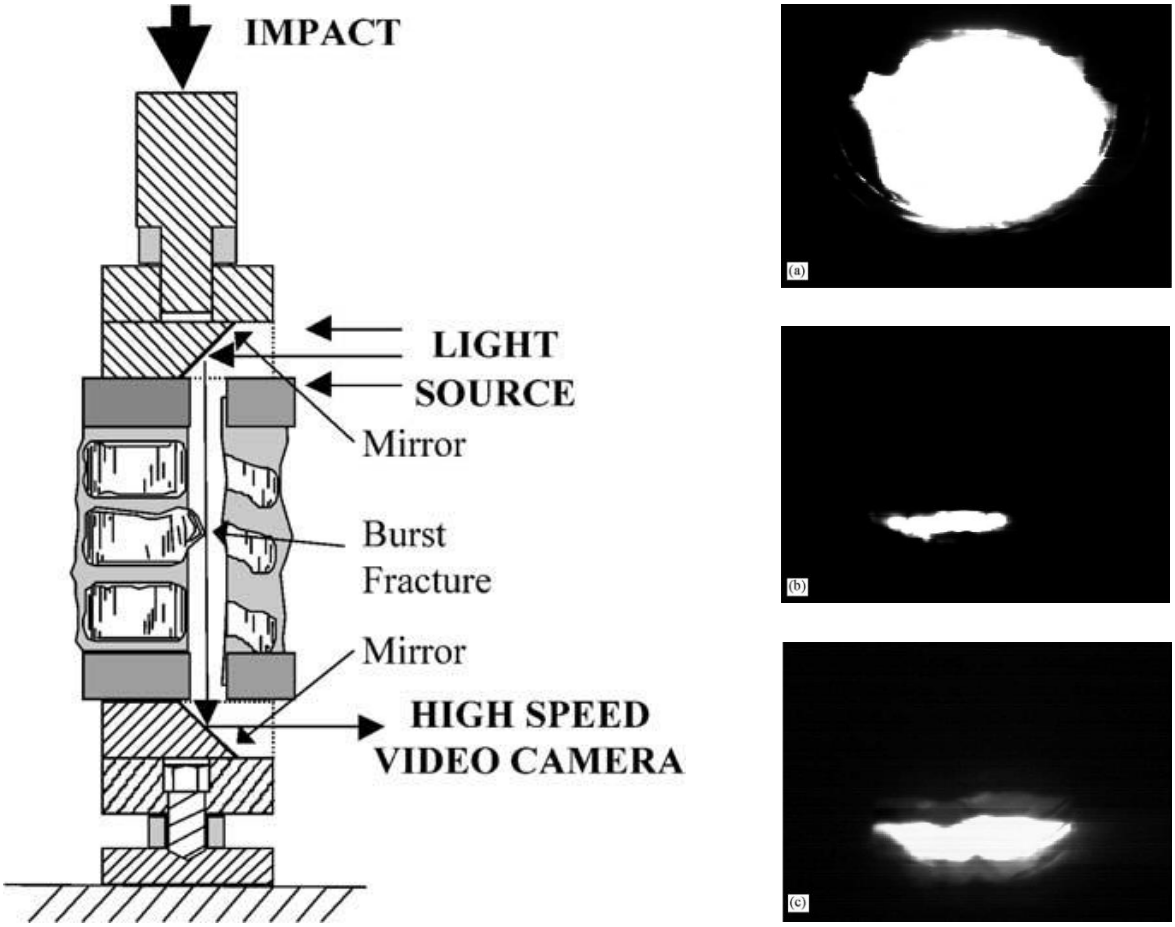

Figure 1-9 Experimental setup used by Wilcox *et al* to image the canal during impact experiments (left). Examples of canal images before injury (top, right), at maximum occlusion (middle, right) and post injury (bottom, right), from Wilcox *et al* study. Figure adapted from Wilcox *et al* [42]. Reprinted from Wilcox, R.K., et al., Measurement of canal occlusion during the thoracolumbar burst fracture process. Journal of Biomechanics, 2002. 35(3): p. 381-4 with permission from Elsevier.

1.3.2 SCOT

The SCOT is an electromechanical transducer developed at the University of Washington to detect geometry changes of the spinal canal [13]. Since its development, SCOTs have been used

in a number of studies investigating the effects of physiologic pure bending loads [12] and combined compression and flexion-extension [35] and lateral bending loads[36].

The SCOT utilises a flexible tubing inserted into the spinal canal and filled with saline. A constant amplitude alternating current (AC) is introduced into the saline at the SCOT excitation element using a constant current driver (CCD). The constant amplitude AC flows through the saline filling the SCOT casing with uniform current density to the ground element at the opposite end to the excitation element of the SCOT. An AC is used so that damage due to deposition and removal of material at the SCOT elements is minimized. Compression of the SCOT casing decreases the cross-sectional area of the saline, resulting in an increase in resistance to the current flow. Since the current field is constant, the increase in resistance is accommodated by an increase in potential difference as described by Ohm's Law (Equation 1-1, where V: potential difference, I: current, R: resistance). Sensing elements spaced 20 mm apart are used to detect the resulting change in potential difference along each segment. The resistance in each segment is a function of the length, cross-sectional area and resistivity of the saline (Equation 1-2, where R: resistance, Δx_k: length of the kth element, A_k: cross-sectional area of the kth element, ρ: resistivity of saline, Figure 1-10).

$$V = IR$$

Equation 1-1 Ohm's Law

$$R = \rho \sum_k \frac{\Delta x_k}{A_k}$$

Equation 1-2 Total resistance in the fluid

A two stage calibration procedure was employed to characterize the SCOT; first the depth of radial compression was correlated with the total cross-sectional area of the casing (saline area and tube wall) quasistatically using CT [13]. The depth of radial compression was then correlated with SCOT voltage during dynamic loading at constant speeds to a fixed depth [13].

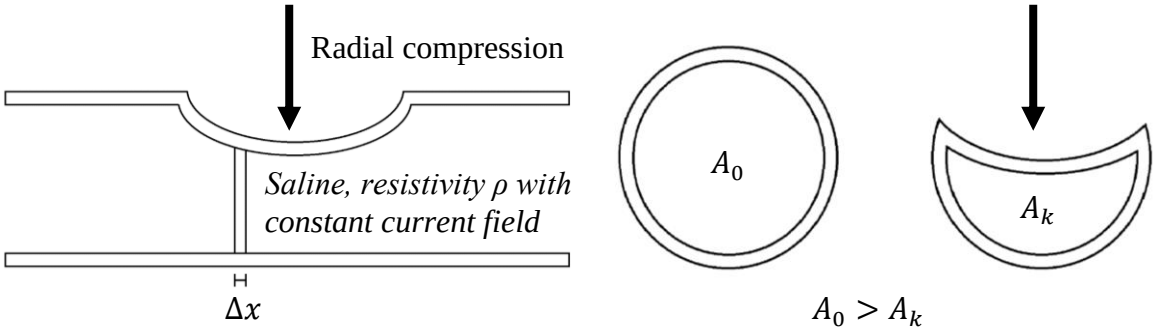

Figure 1-10 Radial compression of the SCOT casing causes a decrease in cross-sectional area

The SCOT developed by Raynak *et al* used thin gauge wire to pierce the SCOT casing and act as the sensing electrodes between which potential differences were recorded (Figure 1-11) [13]. Zhu *et al* later redesigned the sensing electrodes so that the wires were collected and inserted

axially into the SCOT casing [14] (Figure 1-12). This removed the need to pierce the tube and was hoped to be more durable during dynamic impact experiments [14].

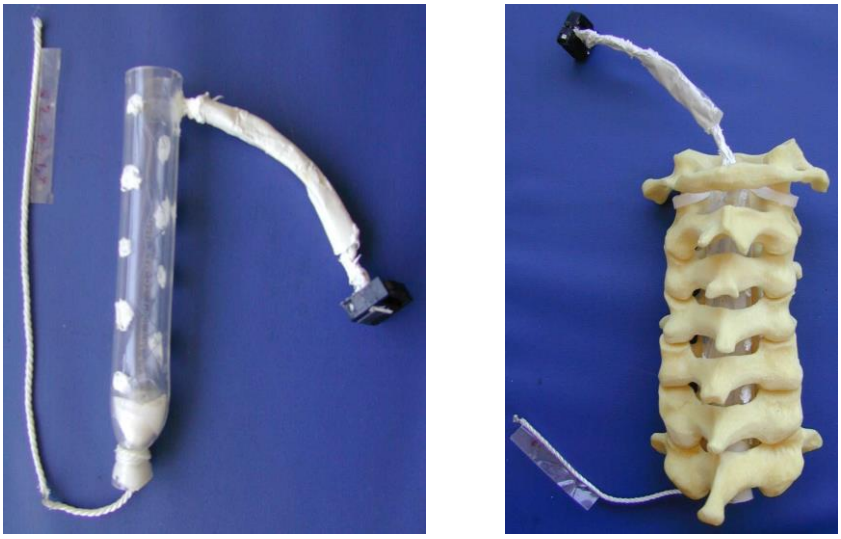

Figure 1-11 Original SCOT developed by Raynak *et al* [13] on its own (left), and inserted into a model of the cervical spine (right) [15]. Reprinted from Van Toen, C., Biomechanics of cervical spine and spinal cord injury under combined axial compression and lateral bending loading, in Mechanical Engineering. 2013, University of British Columbia: University of British Columbia with permission.

Van Toen *et al* used the modified SCOT in a study investigating the effects of lateral eccentricity on the injury biomechanics of the cervical spine under axial compression [36]. Problems with the SCOT instrumentation including corrosion damage to the probe elements, inconsistent SCOT outputs when unloaded and random drops in signal were identified during the study leading to a loss of some data. Furthermore, it was noted that the SCOT required a new characterisation since the redesign of the sensing electrodes [15]. A new characterisation was conducted in our lab (unpublished) and highlighted a decreased resolution of ±15 mm^2 compared to the ±5 mm^2

reported by Raynak *et al* [13], and an accuracy that varied between 1.1 mm^2 and 13.4 mm^2 depending on the shape of the occluder used to deform the tube.

Both iterations of the SCOT have their limitations, particularly with respect to the SCOT casing. The flexible tubing used to contain the saline was chosen so that it would conform to the elliptical shape of the cervical spinal canal; however, this was not typically the case, with the tube filling the canal sagittally, but not laterally [36]. Additionally, the 20 mm length of each detecting segment means the minimum cross-sectional area across that length could be detected, but not its location. Furthermore, while the two part calibration method allows a relationship between SCOT output and TCA to be determined, no such relationship can be found between SCOT output and radial compression. This is because the SCOT output is dependent on the cross-sectional area of the saline carrying the constant current (Equation 1-2), and the cross-sectional area of the saline is a function of both the depth of occlusion, and the shape causing the occlusion (Figure 1-13 and Figure 1-14). Since it cannot be known what the shape of the occluder is that causes the radial compression during impact experiments, no reliable approximation can be made as to the depth of the radial compression.

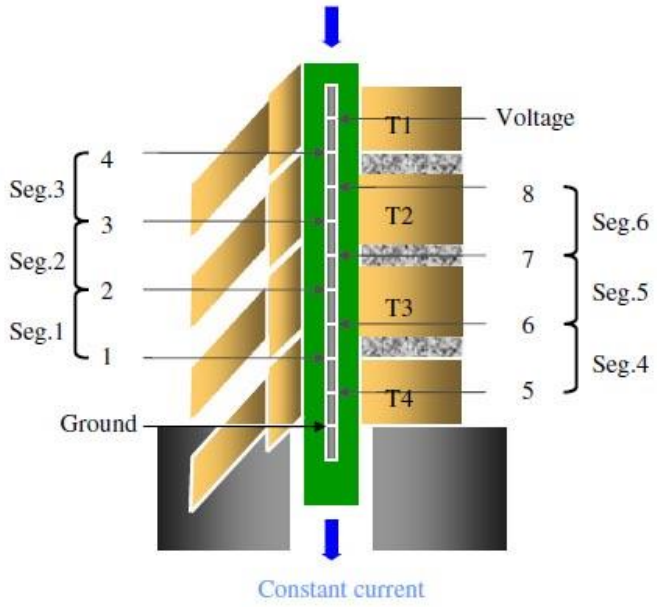

Figure 1-12 Schematic of modified SCOT used by Zhu *et al* with 6 segments used for occlusion detection highlighted [14]. Reprinted from . Zhu, Q., et al., Translational constraint influences dynamic spinal canal occlusion of the thoracic spine: an in vitro experimental study. Journal of Biomechanics, 2008. 41(1): p. 171-9. Epub 2007 Aug 20 with permission from Elsevier.

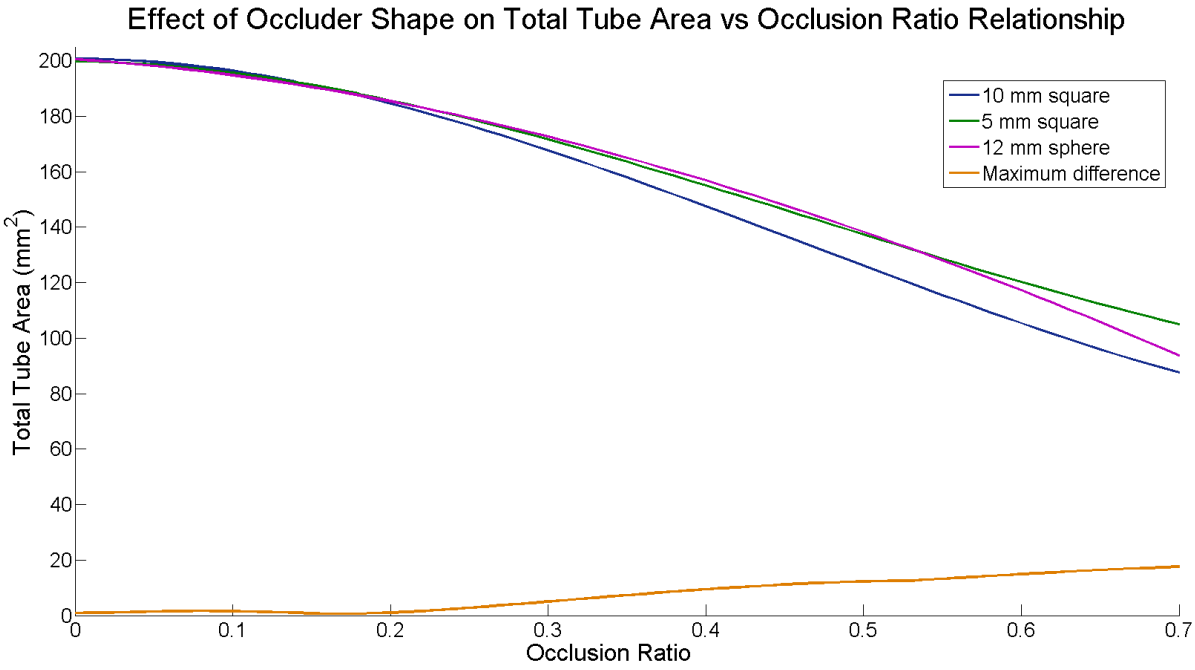

Figure 1-13 Relationship between minimum total cross-sectional area (measured using CT) and occlusion ratio (depth of occlusion divided by the outside diameter of the SCOT casing, 15.9 mm). This data was obtained from a study conducted in our lab and is unpublished (Appendix A).

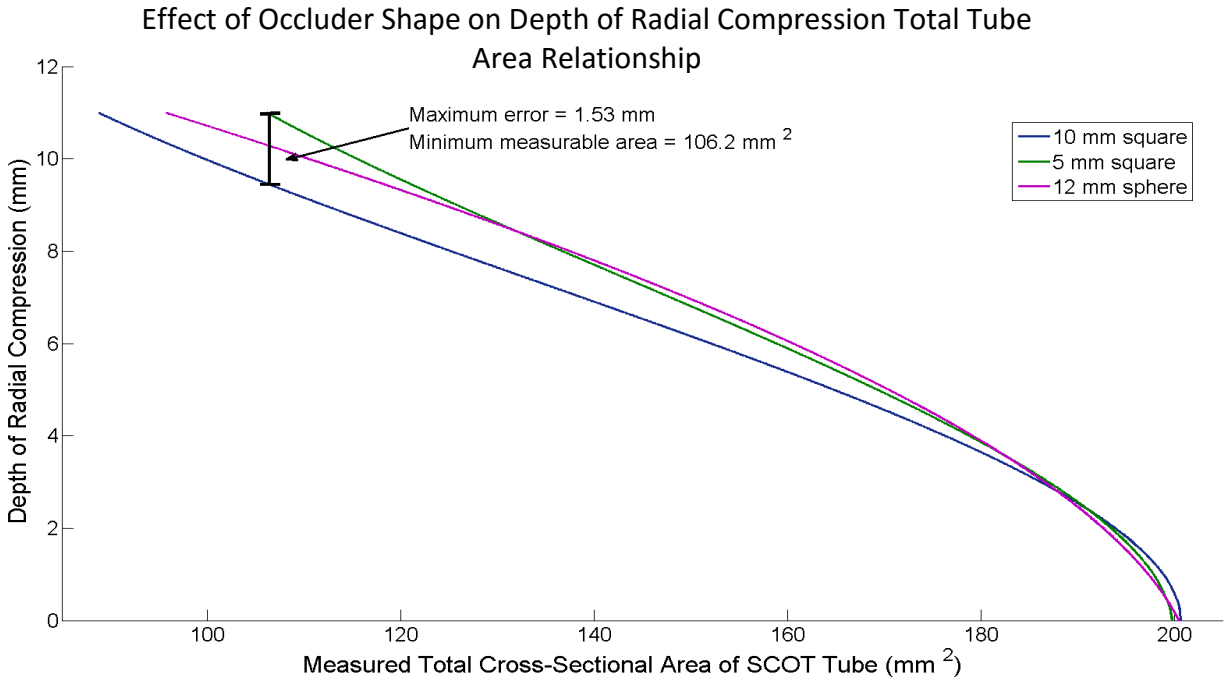

Figure 1-14 Relationship between the depth of radial compression of SCOT tube and the minimum total cross-sectional area (measure using CT). Variation between curves gives a maximum error between the 3 geometries of occluder tested. This data was obtained from a study conducted in our lab and is unpublished (Appendix A).

1.4 Measurement of Canal Occlusion During Bending of the Cervical Spine

Pathologies of acute and degenerative forms of spinal cord impingement can range from radiculopathy to quadriplegia. Upon presentation of such pathologies, imaging investigations provide an indication of the extent of static compression of the spinal cord; however, they do not present an indication of levels of dynamic compression during the injury event. Unfortunately,

existing investigations of dynamic compression of the spinal cord during physiological/non-injurious range of motion (ROM) [12, 43] present an incomplete picture.

Holmes *et al* [43] investigated the changes in canal volume of lower cervical spine segments (C2-C7) during flexion-extension loading. Fresh frozen cadaveric specimens were prepared by removing the spinal cord, leaving the dura mater and other ligamentous tissue intact, and replacing it with a thin-walled latex tube. The tube was sealed at the inferior end of the specimen and connected via plugs and rubber tubing to a graduated cylinder allowing volume changes down to 0.25 ml to be observed. The tube was filled with fluid and a bending force was applied perpendicular to the C2 vertebra in a stepwise manner producing peak bending moments between 0.07 Nm and 0.12 Nm.

Holmes *et al* [43] reported a significant relationship between the angle of flexion (from full extension position) and the change in volume of the canal, with maximum and minimum changes in volume observed being 2.85 ml and 0.75 ml, respectively. Though lateral bending and axial rotation were not investigated directly, the authors described pre-flexing the spine and then applying lateral bending loads by hand to approximately 20 ˚. Changes in volume were reported as approximately 0.2 ml on each side, with a maximum 0.4 ml observed.

Though Holmes and colleagues [43] successfully observed changes in canal volume during stepwise loading, their results are limited. The location of the instantaneous centre of rotation, anterior to the spinal canal [44], results in a lengthening of the spinal canal during flexion and a shortening during extension. These changes in length are accompanied by physiological

lengthening and shortening of the spinal cord [45]. By treating the canal as a single volume, decreases in volume due to localised geometry changes, such as bulging IVDs when loaded in compression, cannot be separated from those due to normal, non-pathological lengthening of the canal.

More recently, Nuckley *et al* [12] used the original SCOT design (described in 1.3.2) from University of Washington [13] to investigate the dynamic changes in canal geometry during normal ROM. Pure bending moments were applied to four-motion segment cadaveric specimens (C3-C7) with a SCOT sensor in place of the spinal cord. A custom load apparatus was used to load specimens in 1 Nm steps to maximum bending moments of 4 Nm in flexion-extension and lateral bending, and 3 Nm in axial rotation. The authors observed measureable changes in the spinal canal midsagittal diameter up to 9.2% reduction during extension; however, these changes were not found to be statistically significant. Furthermore, no significant correlation between occlusion and cervical level was identified.

Nuckley and colleagues [12] highlighted that the SCOT tubing did not fill the canal in the coronal plane, and chose to report the geometry changes in the canal as the changes in midsagittal diameter. The relationship between the midsagittal diameter and cross-sectional area is dependent on the geometry of the object causing the impingement. Since the SCOT measures changes in cross-sectional area of the conducting medium, any relationship to midsagittal diameter will introduce uncertainty relating to the geometry of the impinging object. The authors made efforts to account for this uncertainty by considering 5 mm and 10 mm occluder lengths;

however, this still remains a limitation of reporting midsagittal diameter as a measure of canal occlusion when using a SCOT.

1.5 Objectives

The primary objective of this work was to rebuild and characterize the existing SCOT, incorporating design modifications of the sensing elements and construction to improve durability, consistency and accuracy of TCA measurement. Specific aims for this thesis were to:

1. Design, prototype, build and test a working SCOT
2. Use signal characteristics of the unoccluded SCOT response such as signal to noise ratio (SNR) and variability due to loading of the SCOT as metrics to assess performance of any design modifications incorporated into the rebuilt sensor.
3. Develop a protocol that produced a reasonable and logical quantification of the accuracy of the calibrations performed on the rebuilt SCOT.
4. Demonstrate the use of the SCOT in a flexibility study using subaxial cervical spine segments to investigate the extent of occlusion that can occur during non-injurious bending.

Chapter 2: SCOT Design

2.1 Introduction

The SCOT is a self-contained electromechanical sensor designed to be inserted into the spinal canal to detect geometric changes during biomechanical testing. The SCOT hardware can be divided into two component groups: the mechanical components including the sensor probe and the SCOT tube, and the electrical components including the constant current driver (CCD), and amplification electronics. The existing electrical components, designed and built by Raynak *et al* [13], were confirmed to function as designed, demonstrating stable gains and AC outputs over a range of input frequencies and peak to peak voltages(Appendix B). With the exception of repairing some degraded wiring, the existing electronics were left unchanged. The mechanical components, particularly the exposed loops of copper wire acting as sensing elements, showed significant wear from corrosion (Figure 2-1). This damage necessitated a rebuild of the SCOT, and the opportunity was taken to incorporate design modifications to the mechanical components of the SCOT probe.

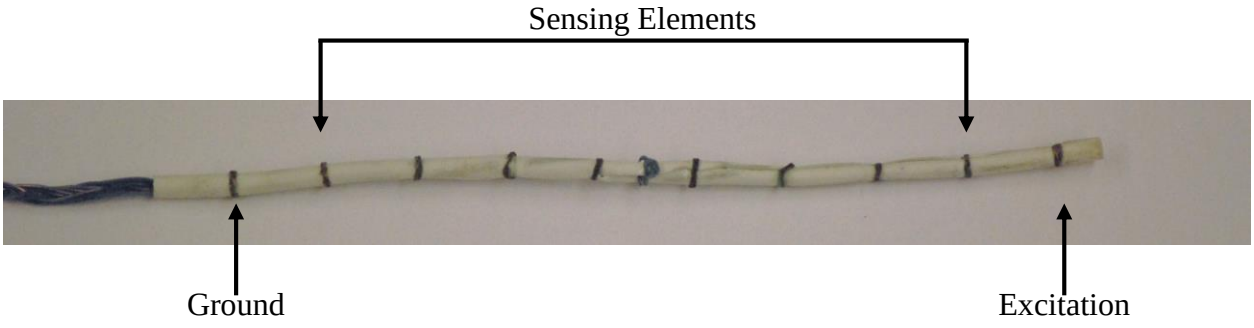

Figure 2-1 Image of existing SCOT with loops of 31 AWG wire as sensing elements and source and sink elements. Refer to Figure 1-12 for schematic of probe with definitions of each segment / element type.

2.2 Design Criteria

The SCOT has been rebuilt for testing of the cervical spine when subjected to dynamic axial compression at various lateral eccentricities. This is a continuing phase of the project initiated by Carolyn Van Toen [15]. The study being conducted will take place over several weeks, requiring the SCOT probe to be tough and durable, demonstrating a high signal performance and accuracy despite being exposed to high energy loading (when in the spinal canal). Modifications to the existing Zhu *et al* [14] iteration of the SCOT aimed to improve durability without significantly affecting performance. In particular, SNR and consistency of the unoccluded response of the SCOT before and after loading were considered as measures to compare the existing SCOT and the new SCOT performance. Stability of the unoccluded SCOT was defined as the absolute value of the difference between the unoccluded SCOT output before and after loading during calibration normalized to the increase in SCOT response when loaded, expressed as a percentage (Equation 2-1). The SNR was calculated as the ratio of the mean increase in signal output when loaded to the standard deviation of the output when unloaded during calibration, converted to decibels (Equation 2-2). A summary of the signal characteristics of the existing SCOT modified by Zhu *et al* [14] and used by Van Toen *et al* [36] is presented in Table 2-1.

$$|dV_{RMS}| = \frac{\left|\mu_{V_{RMS,post}} - \mu_{V_{RMS,pre}}\right|}{\mu_{V_{RMS,loaded}} - \mu_{V_{RMS,pre}}} \times 100\%$$

Equation 2-1 Definition of consistency of unoccluded SCOT output (where $\mu_{V_{RMS,pre}}$ and $\mu_{V_{RMS,post}}$ are the unoccluded mean of the root mean square voltage outputs before and after loading during calibration, respectively, and $\mu_{V_{RMS,loaded}}$ is the mean of the root mean square voltage output when loaded)

$$SNR_{dB} = 10\log_{10}\left(\frac{\mu_{V_{RMS,loaded}} - \mu_{V_{RMS,pre}}}{\sigma_{V_{RMS,unloaded}}}\right)^2$$

Equation 2-2 Definition of SNR (in decibels) (where $\mu_{VRMS,\ loaded}$, $\mu_{VRMS,\ pre}$ and $\sigma_{VRMS,\ unloaded}$ are the mean root mean square voltage output when loaded, the root mean square voltage output before loading and standard deviation of root mean square voltage output when unloaded during calibration, respectively)

Table 2-1 Signal characteristics of existing SCOT as used by Zhu *et al* [14] and Van Toen *et al* [36]. Data obtained from characterization study conducted in laboratory (Appendix A).

Input Signal Properties					
V_{PP} (V)	**f (kHz)**	**$\mu_{SNR_{dB}}$(dB)**	**$\sigma_{SNR_{dB}}$(dB)**	**$\mu_{dV_{RMS}}$(%)**	**$\sigma_{dV_{RMS}}$(%)**
1.0	2.0	69.7	4.3	0.06	0.04

The following design criteria were considered when incorporating modifications into the rebuilt SCOT:

1. The SCOT must continue to be usable with the existing electronics.
2. The SCOT must incorporate materials that can resist degradation due to corrosion.
3. The SCOT should function with an SNR_{dB} and dV_{RMS} that matches or exceeds the performance of the original SCOT.

2.3 Design Theory

As described in section 1.3.2, the SCOT is a resistance based sensor designed to detect geometric changes of the spinal canal by measuring geometric changes of the SCOT casing inserted into it. The SCOT casing is filled with a conducting fluid and a constant amplitude AC field is produced between the ground and excitation elements (Figure 2-1). Changes in geometry result in changes to the resistance to current flow in the conducting fluid filling the SCOT casing. Sensing

elements spaced evenly between the ground and excitation elements form overlapping segments. Changes in voltage between the sensing elements that make up each SCOT segment are used to determine the total resistance to current flow along the SCOT segment.

Fundamental to the functionality of the SCOT is the production of a uniform constant current field in the conducting fluid. If the current field produced in the fluid were not uniform throughout the saline, then the relationship between cross-sectional area of the current flow and the resistance to current flow (Equation 1-2) would not apply. Calibration of the SCOT is performed to determine the relationship between segment change in voltage and the minimum cross-sectional area of the segment; however, to be able to perform tests using the calibration, the current field produced in the conducting fluid for the tests would have to match the current field produced during calibration. Thus, a uniform constant current field in the conducting fluid is desired so that the applicability of the SCOT calibration is maintained for tests.

Since the SCOT electronics hardware were confirmed to function as they were intended when built by Raynak *et al* [13] (constant current and voltage gains, Appendix B), modifications to improve the SCOT probe were focussed on ensuring a consistent uniform current field could be produced in the conducting fluid. This was approached by considering the geometry of the sensing elements. Field lines are used to describe the electric field created by charged particles or surfaces. A charged particle placed in the electric field would experience an electromagnetic force tangent to the field line at that point. In the case of the SCOT, the medium filling the space between the conducting elements is a conducting fluid consisting of ions, thus the field lines represent the direction of current flow. Field lines exit and enter conducting elements

perpendicular to their surface. Spherical sensing, ground and excitation elements allowed greater surface area when compared to the exposed copper wires. Spherical and cylindrical geometries were considered in the new SCOT design to improve uniformity and consistency of the constant current field created in the conducting fluid. Furthermore, by changing the surface geometry of the conducting elements, the distribution of field lines is altered (Figure 2-2) and can also have an effect on the uniformity of the constant current field created. Ultimately, only the spherical element design was considered since the cylindrical element design was deemed too difficult to manufacture.

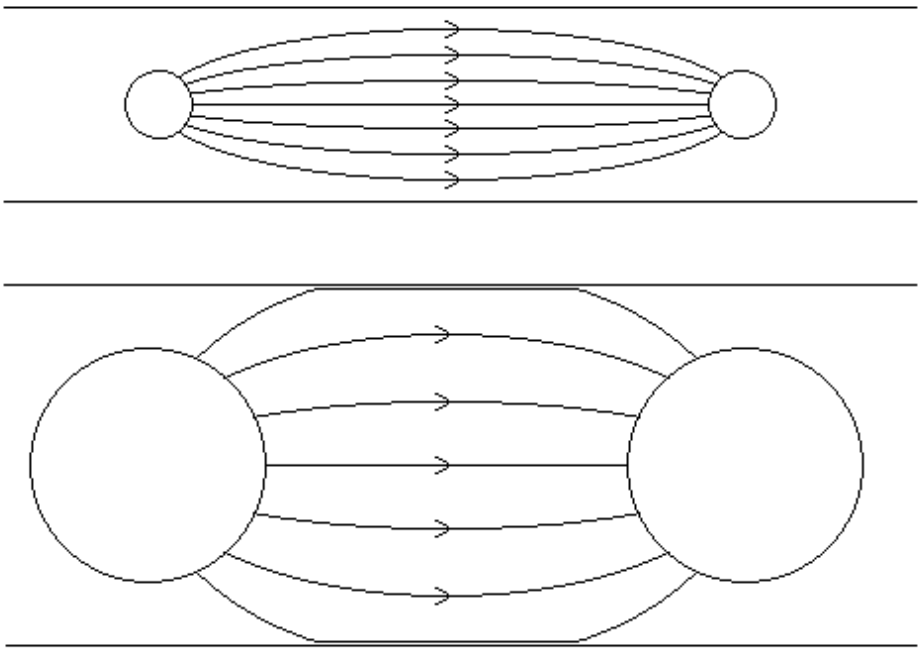

Figure 2-2 Examples of electric field lines between spheres of different sizes, but same net charge. The horizontal lines represent the edges of the SCOT casing which constrain the fluid and electric field NB. The loops of wire used by Zhu *et al* [14] would produce field lines similar to those in the top schematic.

+ -

Finally, for all prototypes, a sponge was inserted into the SCOT casing to sit immediately superior to the ground SS ball bearing and hold the probe in the centre of the SCOT casing. Similarly, an end plug was designed to hold the SCOT probe in the centre of the SCOT casing, inferior to the excitation stainless steel (SS) ball bearing (Figure 2-5). By including these contingencies in the SCOT testing protocol, a more consistent location of the SCOT probe in the casing between tests was achieved, reducing one source of variability for the current field produced in the saline.

2.4 Design Prototypes

The configuration of the SCOT probe, consisting of 8 sensing elements, a ground element and an excitation element remained unchanged so that it could continue to be used with the existing electronics. In order to address the design criteria 2 and 3, the geometry and materials of the probe components, and the method used to form electrical connections with the existing electronics were considered.

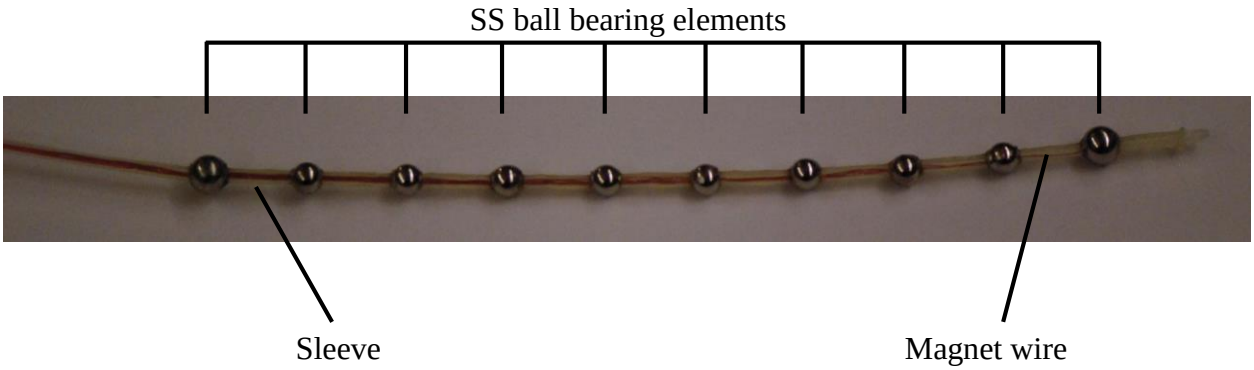

Figure 2-3 Image of SCOT prototype highlighting the general design elements of the modified SCOT

The new design used ball bearings with holes drilled through their centre threaded in a similar fashion as beads onto a sleeve with an outer diameter of 1.59 mm. The ball bearings used were 316 SS ball bearings to improve corrosion resistance. Running through the sleeve were 10 enameled magnet wires with diameter 0.122 mm (38 AWG) (Soderon 155, Superior Essex Inc., Atlanta, GA), each exiting the sleeve via a small hole and connecting to a single SS ball bearing element. An example of a prototype using this design is presented in Figure 2-3. A total of 3 SS ball bearing sizes, two types of sleeve material, and two different methods for forming the electrical connection between the magnet wire and the SS ball bearing elements were investigated.

It was hypothesized that using larger diameter SS ball bearings for the ground and excitation elements would result in a more uniform electric field being generated in the fluid; however, small diameter sensing elements were desired to maximize the amount of possible deformation of the SCOT casing before they came into contact with each other. It was hoped that a combination of SS ball bearing would satisfy both requirements and would ensure a uniform current field and maximum possible range of detectable occlusions. Ultimately, the size of the sensing elements was restricted by practical considerations, as they became increasingly difficult to machine as their diameter was decreased beyond 3.18 mm. Similarly, the maximum size of the ground and excitation elements was limited by the inner diameter of the SCOT casing.

Toughness and size were important considerations when considering possible sleeve materials. A minimum outer diameter was desired so that maximum surface area of the SS ball bearings could be obtained (drilling through their middle reduces total surface area); however, it was important

to ensure the inner diameter was large enough to accommodate 10 magnet wires. Furthermore, since the magnet wires were required to be threaded through the small holes where each of sensing, ground and excitation elements were located, a larger internal diameter was desirable.

Electrical connections between the SS ball bearing element and the magnet wire were formed by either soldering the wire directly or bonding the wire using a silver doped epoxy (SDE) (Loctite 3888, Henkel AG & Co. KGaA, Dusseldorf, Germany). Both methods required the magnet wire to exit the sleeve, underneath where the SS ball bearing would sit, via a small hole punctured in the sleeve. When soldering the magnet wire to the SS ball bearing, the magnet wire would be pulled through a 0.66 mm diameter hole drilled at 45 ˚ to meet the central hole (through which the sleeve threads). Solder was then used to fill the 45 ˚ hole and form an electrical connection with the magnet wire (Figure 2-4, A). When using SDE for the electrical connection, the stripped magnet wire pulled out of the sleeve would be encased in SDE and the SS ball bearing slid over top of it and allowed to cure (Figure 2-4, B). Regardless of the method used to form the electrical

connection, a general purpose coating (M-Coat A, Vishay Precision Group, Malvern, PA) was used to seal any gaps between the sleeve and the SS ball bearings and hold them in place.

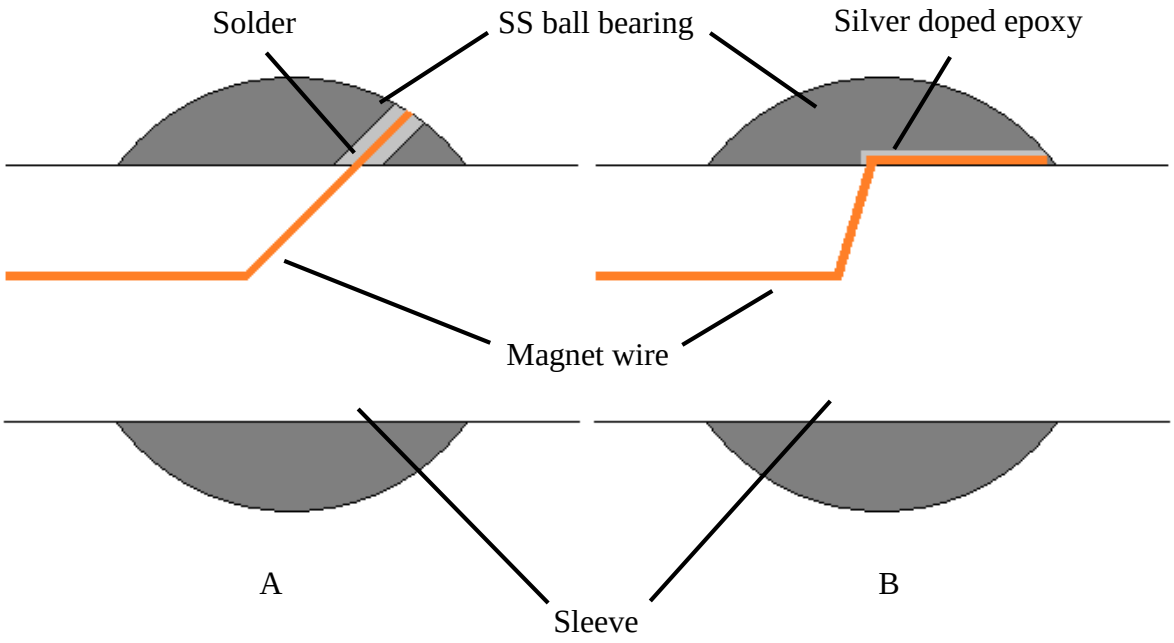

Figure 2-4 Illustration of soldering technique (A) and silver doped epoxy technique (B) for connecting magnet wires to the SS sensing, excitation and ground elements.

A total of six prototypes were developed and built for testing. Table 2-2 presents a summary of the prototypes, as well as the original SCOT for comparison.

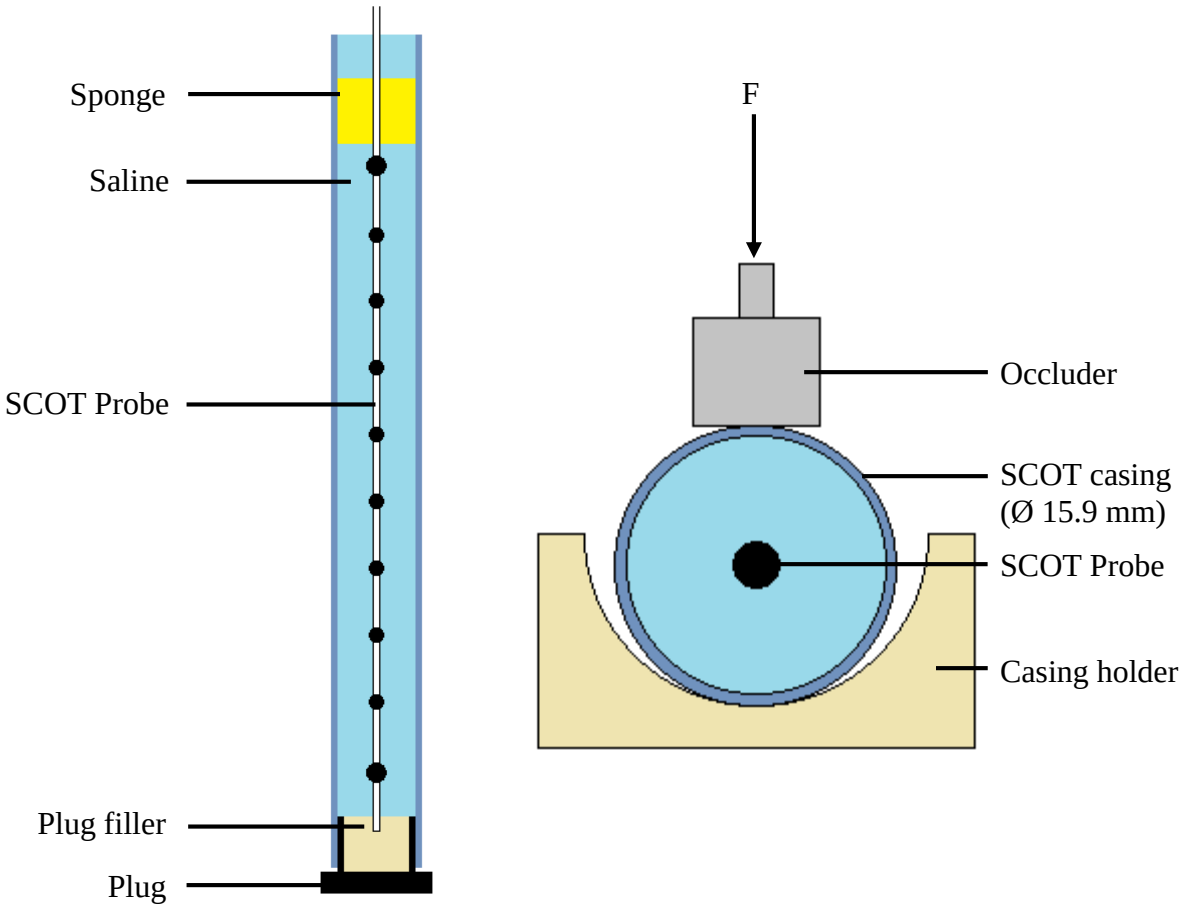

Figure 2-5 Illustration of use of sponge and custom plug to hold SCOT probe in the centre of the SCOT casing (left); axial view of SCOT casing and probe with occluder used to apply radial compression for performance testing (right).

2.5 Design Evaluation

2.5.1 Methods

In order to evaluate the performance of the SCOT prototypes against the design criteria, standardized testing was performed. Results from these tests were used to decide on the final design for the rebuilt SCOT.

Table 2-2 Summary of the components for all six prototypes and the original SCOT. No electrical connection type is listed for SCOT original as it used continuous wires (SWI = standard wire insulation, SDE = silver doped epoxy, HS = heat shrink

Sensor	Excitation / Ground Element	Sensing Element	Electrical Connection	Sleeve material
SCOT original	2 loops 31 AWG wire	2 loops 31 AWG wire	NA	SWI
SCOT v1	Ø 3.97 mm SS ball	Ø 3.97 mm SS ball	Solder	SWI
SCOT v2	Ø 3.97 mm SS ball	Ø 3.18 mm SS ball	SDE	SWI
SCOT v3	Ø 3.97 mm SS ball	Ø 3.18 mm SS ball	SDE	HS
SCOT v4	Ø 3.97 mm SS ball	Ø 3.18 mm SS ball	SDE + Solder	HS
SCOT v5	Ø 6.35 mm SS ball	Ø 3.18 mm SS ball	Solder	HS
SCOT v6	Ø 3.97 mm SS ball	Ø 3.18 mm SS ball	Solder	HS

2.5.1.1 Loading

Each prototype probe was tested with standard SCOT casings (Ø 15.9 mm Tygon R-1000, Norton Performance Plastics, Canton, OH) filled with saline (0.9% wt.). Probes underwent the same load protocol applied to a single segment (SCOT 1), repeated 6 times. After a 5 second hold at 0 mm compression, the SCOT segment was loaded in radial compression over the centre of the segment to a maximum depth of 8 mm at a rate of 2 mm/s using a materials testing machine (FastTrack 8800 Dynamight, Instron, Canton, MA). The segment was held at 8 mm compression for 5 seconds, then unloaded at 2 mm/s to 0 mm compression and held unloaded for 5 seconds. A 10 mm × 10 mm square occluder was used to compress the SCOT casing against a casing holder designed to mimic the curvature of the posterior arch of the spinal canal [13] (Figure 2-5).

2.5.1.2 Instrumentation and Data Acquisition

Each prototype SCOT probe was connected to the existing electronics. The SCOT input signal was a continuous sine wave with frequency 2 kHz and peak to peak amplitude of 1 V_{pp}. If the

prototype probe continued to function as designed throughout testing with these input conditions, then an increased input frequency and peak to peak voltage of 3 kHz and 1.5 V_{pp}. was tested, respectively. The increased amplitude AC was used to ensure resolution of the probe was maximized by using the entire range of the data acquisition system signal input. By increasing the frequency of the AC, the response to changes in geometry of the saline was increased, since the AC peaks happened more often. A custom LabVIEW program (National Instruments, Austin, TX) was used to collect SCOT output signals for all segments as well as the LVDT from the materials testing machine using a modular high speed data acquisition (DAQ) system (cDAQ 9172 with NI9215 modules, National Instruments, Austin, TX) at a sample frequency of 50 kHz.

2.5.1.3 Data Analysis

Custom MATLAB code (version 7.13.0.564, MathWorks Inc., Natick, MA) was used for all data analysis. Displacement data was zeroed and low-pass filtered (second order, Butterworth, 100 Hz cut off) and raw SCOT outputs were low-pass filtered to remove direct current offset (second order, Butterworth, 120 Hz cut off). SCOT segments were defined according to Figure 2-6. Filtered SCOT segment outputs were converted to root mean square (RMS) voltages using a RMS sampling frequency of 100 Hz (equivalent to 500 data points per calculation with 50 kHz data collection rate). The middle 5000 data points for each of the unloaded 5 second holds in the load protocol were used to calculate the SNR_{dB} (Equation 2-2) and dV_{RMS} (Equation 2-1). The survivability (if it still worked after loading) and performance of each prototype were compared against the original SCOT. The SNR_{dB} and dV_{RMS} metrics were then used to decide on the final design of the modified SCOT probe.

2.5.2 Results

A typical plot of displacement and SCOT segment RMS voltage outputs for the testing is presented in Figure 2-7. Of the 6 prototypes produced, only SCOT v6 remained undamaged throughout testing, thus it was the only prototype tested at a higher input amplitude and frequency (1.5 V_{pp} at 3 kHz). A summary of the performance of each prototype, as well as the original SCOT is presented inTable 2-3.

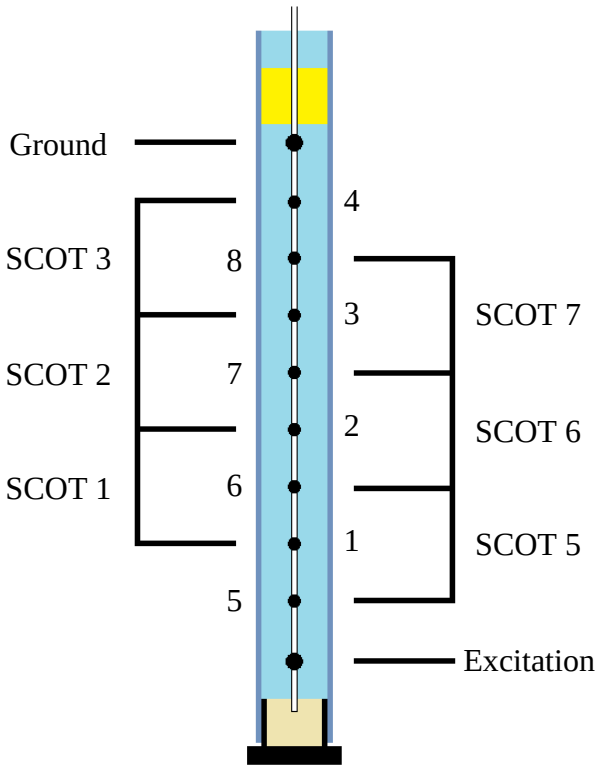

Figure 2-6 SCOT segment naming and element numbering conventions. SCOT segment 4, defined as the voltage difference between ball4 and 5 is omitted as it encompasses the entire length of the SCOT casing.

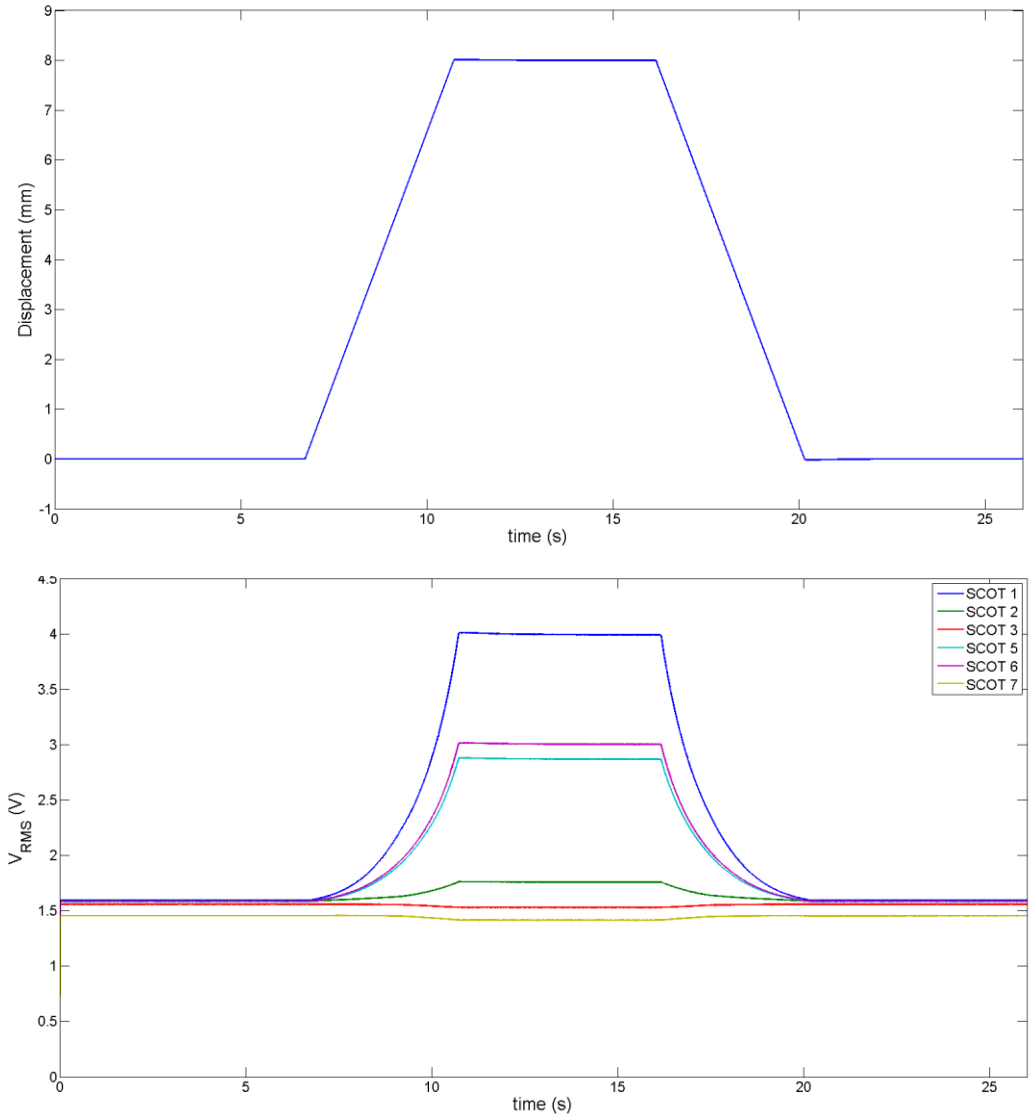

Figure 2-7 Typical plots of displacement (top) and V_{RMS} (bottom) for a standardized test of SCOT v6

Table 2-3 Summary of results from standardized testing of SCOT prototypes and the original SCOT (* data for original SCOT had already been obtained from a previous calibration conducted in the lab).

Sensor	Input signal	$\mu_{SNR_{dB}}$	$\sigma_{SNR_{dB}}$	$\mu_{\lvert dV_{RMS}\rvert}$(%)	$\sigma_{\lvert dV_{RMS}\rvert}$(%)	Notes
SCOT original*	1 V_{pp} @ 2 kHz	69.7	4.3	0.06	0.04	-
SCOT v1	1 V_{pp} @ 2 kHz	-	-	-	-	• Fatigue of sleeve material caused failure
SCOT v2	1 V_{pp} @ 2 kHz	-	-	-	-	• Fatigue of sleeve material caused failure
SCOT v3	1 V_{pp} @ 2 kHz	-	-	-	-	• Failure at electrical connection
SCOT v4	1 V_{pp} @ 2 kHz	73.3	0.3	0.07	0.01	• Failure at electrical connection • Water damage
SCOT v5	1 V_{pp} @ 2 kHz	73.1	2.0	0.10	0.05	• Failure at electrical connection • Water damage
SCOT v6	1 V_{pp} @ 2 kHz	73.3	1.9	0.10	0.14	-
SCOT v6	1.5 V_{pp} @ 3 kHz	78.0	2.4	0.05	0.08	-

2.5.3 Discussion

A total of 6 prototype SCOT probes were designed, constructed and then evaluated against the original SCOT. Typically, probes constructed using standard wire insulation were not durable enough to withstand the direct repeated loading employed in the load protocol and typically failed at the sensor element locations. Probes constructed with an activated heat shrink sleeve were more durable and did not experience failure. All probes constructed using SDE as a form of electrical connection failed either at the connection or due to water damage. It is likely the incomplete bond between the magnet wire and the SS ball bearing elements hindered the effectiveness of the sealant used for water proofing.

Only the SCOT v6 probe proved able to withstand the loading protocol without failure. The SCOT v6 probe demonstrated an improved SNR_{dB} when compared with the original SCOT. Consistency of unloaded SCOT response before and after loading was found to be less than 1% of the change in SCOT response when loaded and was considered satisfactory for all iterations of the SCOT tested. It was decided to proceed with the SCOT v6 probe due to its ability to withstand multiple tests involving direct loading of the probe and its comparable signal characteristics with the original SCOT.

The method that has been employed to evaluate the SCOT designs has its weaknesses. Ideally, a more thorough repetitive loading protocol would have been utilized to assess the long term durability of each design. Failures due to waterproofing and impact resistance were identifiable soon into the testing protocol; however, long term durability in regards to corrosion resistance remains unexamined. Furthermore, testing of the SCOT at speeds only up to 150 mm/s during

these initial tests gave an incomplete view of both the signal response characteristics and the durability of the probe itself, particularly when its design intent was for experiments at higher energies.

2.6 Design Conclusions

The final design was the SCOT v6 prototype. This design consisted of a sleeve constructed from heat shrink (Modified polyvinylidene fluoride, 3M, St. Paul, MN), ground and excitation elements made from 3.97 mm diameter 316 SS ball bearings, and sensing elements made from 3.18 mm diameter 316 SS ball bearings. Electrical connections between sensing and ground and excitation elements were soldered, with details of the method outlined in Appendix C . The final design was able to withstand multiple loading cycles up to 150 mm/s (Chapter 3:) during calibration and has since been tested up to 2000 mm/s without failure (Appendix D) using a congruent loading protocol. Since only 316 grade SS and plastic materials are exposed to the saline during normal use, in conjunction with extensive water proofing, the newly designed SCOT should prove to be more resistant to corrosive wear than previous iterations. The modified design has been shown to function as originally intended at an increased input signal frequency and peak to peak voltage. The increased peak to peak input voltage allows the entire measurement range of the data acquisition system to be used throughout the range of occlusions the SCOT can detect. Consequently, the resolution of the measurements that can be made has been improved. The SNR for the modified SCOT exceeded that of the existing SCOT, when using identical input signal conditions (73.3 dB versus 69.7 dB), suggesting a reduction in input noise over the signal range during loading. These effects were magnified further when the peak to peak voltage of the input signal was increased (73.3 dB at 1 V_{pp} versus 78.0 at 1.5 V_{pp}). With

these points in mind, the newly designed SCOT probe satisfies all design criteria and once calibrated, can be used with existing electronics for future experiments.

Chapter 3: Characterisation of the Modified SCOT

3.1 Introduction

The implementation of design modifications to the original SCOT designs [13, 14] necessitated a new characterisation of the SCOT. The opportunity was taken to investigate the calibration method used to characterise the SCOT in terms of its physical relevance to the theory being applied and the consistency of calibration produced. This ultimately led to a new approach to defining the accuracy of the SCOT that is directly related to the consistency of calibration.

Raynak *et al* [13] described a two stage calibration method to characterise the SCOT. First, a 3rd order polynomial was used to correlate the depth of radial compression to the TCA (saline area and tube wall) of the SCOT casing quasistatically using CT [13]. The depth of radial compression was then correlated with the SCOT output during dynamic loading at fixed speeds to a predetermined depth. Finally, a 5th order polynomial was fitted between the SCOT output and the TCA at given radial displacements (Figure 3-1).

The calibration method used by Raynak *et al* [13] was limited due to the dependence of the geometry of the occluder used to compress the SCOT, on the resultant TCA. That is, for a given depth of radial compression, a large occluder would result in a smaller TCA compared to a small occluder. Raynak *et al* tested two sizes of occluder (5 mm and 10 mm length) and used the maximum difference between TCAs at a given theoretical SCOT output to define the resolution. Other parameters used to characterize the original SCOT included [13]:

- Functional range: TCA limits over which the SCOT could operate,

- Threshold: the smallest TCA for which the observed SCOT output and theoretical SCOT output coincided,
- Sensitivity: the slope of the curve correlating SCOT output to TCA, and
- Dynamic response: qualitative description of the effects of varying speeds on the response of the SCOT output.

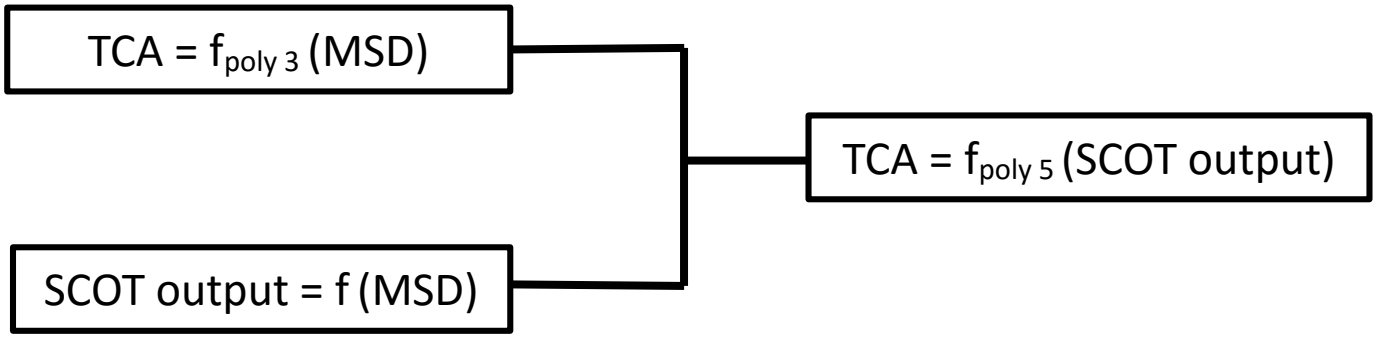

Figure 3-1 Block diagram illustrating the work flow of the two stage calibration method used for characterisation of SCOT (where MSD is mid sagittal displacement, or depth of radial compression and TCA is total cross-sectional area). NB. No function is fitted relating SCOT output to MSD; instead the MSD is converted to TCA using $f_{poly\ 3}$, and then $f_{poly\ 5}$ relates TCA to SCOT output.

The following methods section describes a similar two stage calibration process to characterise the modified SCOT; however, a different approach to the data analysis was employed in an effort to simplify and streamline the calculation of error associated with the SCOT measurements.

3.2 Methods

3.2.1 Static Calibration

A static calibration was used primarily to describe the relationship between the depth of radial compression, the shape of the occluder, and the resultant TCA of the SCOT. Secondary to this,

the static calibration gave the maximum radial compression the SCOT casing could undergo before the SCOT probe was being directly compressed into the SCOT casing wall, and its readings could no longer be considered accurate.

The static calibration consisted of loading the SCOT at fixed depths and then imaging it using CT (200 ms integration time; 41 μm resolution). A single SCOT segment was loaded using two occluder sizes (5 mm × 5 mm and 10 mm × 10 mm). Software (Analyze 12.0, Analyze Direct Inc., KS, U.S.A.) was used to isolate the SCOT segment tested, then measure the TCA (SCOT casing and saline area) for each slice at each depth of occlusion, and check if the probe was being compressed into the SCOT casing wall. A third order polynomial was fitted to correlate minimum TCA of the SCOT segment at each depth of occlusion.

A static calibration using the Zhu *et al* [14] SCOT iteration had previously been performed in our lab in August 2013 (Appendix A), and the relationship between the depth of radial compression, the shape of the occluder, and the resultant TCA of the SCOT already described. Since the same material SCOT casing was being used with the new SCOT, it was assumed that these relationships would remain unchanged from what was determined previously. For the new SCOT, static calibration was only required to determine the minimum TCA (as a result of radial compression) possible before contact between the SCOT probes and casing wall occurred. For this reason, only a static calibration using the 10 mm × 10 mm occluder was performed, since it was the geometry responsible for the largest reductions in TCA for the minimum radial compression (i.e. worst case scenario). Imaging software (ImageJ version 1.50b, Wayne Rasband, National Institutes of Health, U.S.A.) was used to trace the outline of the SCOT casing

and measure the TCA. This measurement was repeated 6 times and the average of measurements taken to be the minimum TCA measureable.

3.2.2 Dynamic Calibration

A similar load protocol to that described in Chapter 2: was adopted for the characterisation of the modified SCOT. Each segment of the probe was tested using a standard SCOT casing (Tygon R-1000, Norton Performance Plastics, Canton, OH) filled with saline (0.9 %wt.). After a 5 second hold at 0 mm compression, the SCOT segment being calibrated was loaded at its centre in radial compression to a maximum depth of 8 mm, at either 2 mm/s or 150 mm/s using a materials testing machine (FastTrack 8800 Dynamight, Instron, Canton MA) (Figure 3-2). The segment was held at 8 mm compression for 5 seconds and then unloaded at the same rate it was loaded, and held for a further 5 seconds at 0 mm compression. Each segment calibrated (6 total, SCOT 1-3, SCOT5-7, Figure 2-6) was tested 4 times using two occluder sizes (5 mm × 5 mm and 10 mm × 10 mm) at 2 mm/s and 150 mm/s (total 96 trials). Calibrations were conducted before use each day throughout the flexibility study described in Chapter 4:, allowing an assessment of consistency of calibration with respect to time.

3.2.3 Data Analysis

The load step from the last three trials of each load condition (speed and occluder shape) was analysed using custom MATLAB code (version 7.13.0.564, MathWorks Inc., Natick, MA). Conditioning of the SCOT outputs and materials testing machine displacement data was congruent with that described in Chapter 2:. First displacement data from the materials testing machine was zeroed and low-pass filtered (second order, Butterworth, 100 Hz cut off). SCOT

segment output voltages were low-pass filtered to remove direct current offset (second order, Butterworth, 120 Hz cut off) and then converted to RMS voltages using a sampling frequency of 100 Hz (equivalent to 500 data points per calculation with 50 kHz data collection rate).

The radial displacement data from the materials testing machine was then converted to a TCA value according to the existing 3rd order polynomial relationship determined from the static calibration (Equation 3-1, Equation 3-2 and Equation 3-3).

$$TCA_{10sq}(r) = 337.4r^3 - 466.0r^2 - 0.8358r + 200.7$$

Equation 3-1 Existing 3rd order polynomials used to convert radial displacement data to TCA when using a 10 mm × 10 mm square occluder (where r is the occlusion ratio, that is, the depth of radial compression divided by the unoccluded outer diameter of the SCOT casing)

$$TCA_{5sq}(r) = 265.9r^3 - 360.4r^2 - 8.875r + 199.8$$

Equation 3-2 Existing 3rd order polynomials used to convert radial displacement data to TCA when using a 5 mm × 5 mm square occluder (where r is the occlusion ratio, that is, the depth of radial compression divided by the unoccluded outer diameter of the SCOT casing)

$$TCA_{ss}(r) = 46.73r^3 - 195.6r^2 - 38.51r + 200.5$$

Equation 3-3 Existing 3rd order polynomials used to convert radial displacement data to TCA when using a 12 mm diameter spherical occluder (where r is the occlusion ratio, that is, the depth of radial compression divided by the unoccluded outer diameter of the SCOT casing)

Calibration curves were produced to describe the TCA fitted with the static calibration as a function of the SCOT RMS voltage using the relationship:

$$TCA = \frac{a}{SCOT_{RMS}} + b$$

Equation 3-4 Function used to fit the total cross-sectional area (TCA) as a function of SCOT RMS voltage ($SCOT_{RMS}$), where a and b are fit constants.

Contrary to the 5th order polynomial fits used by Raynak *et al* [13], the function described by Equation 3-4 was chosen to describe the relationship between TCA and SCOT RMS as it was more in line with the theoretical description of the relationship (Equation 1-1and Equation 1-2). The benefit of this approach was a more physically relevant description of the SCOT calibration.

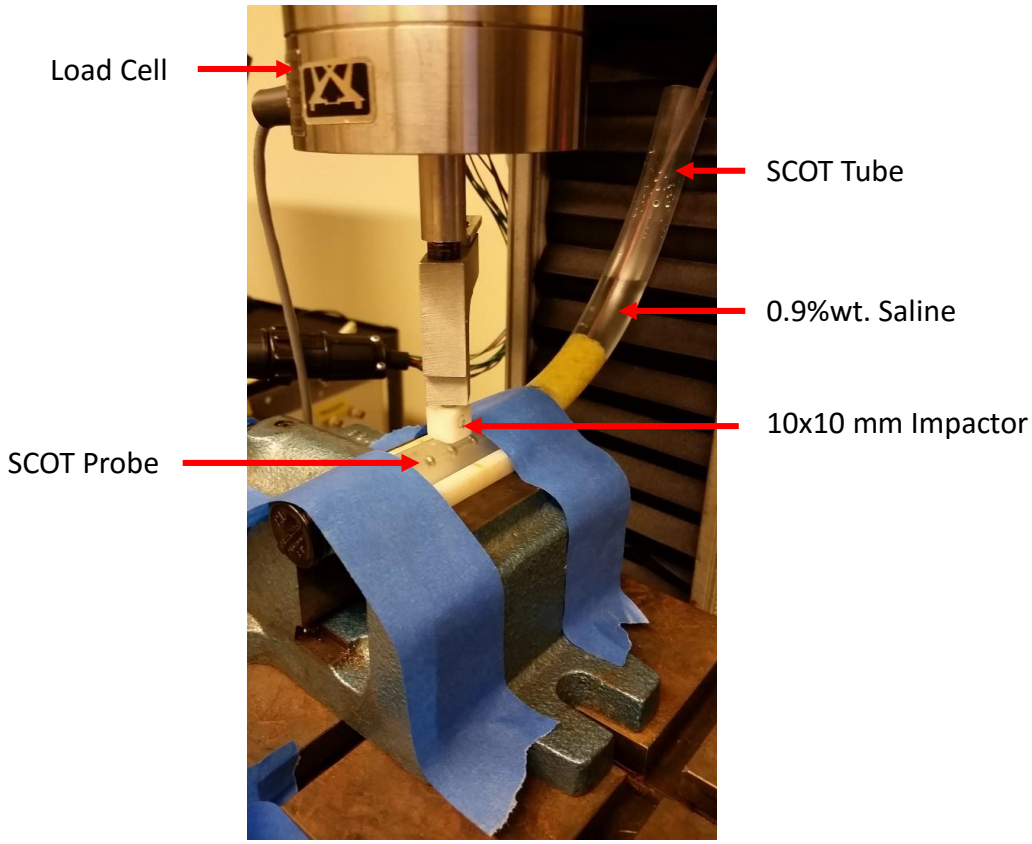

Figure 3-2 Image of the experimental setup used for dynamic calibration

A calibration curve was produced for each of the three trials analysed for each load condition. The three calibration curves were then averaged, resulting in a single calibration curve for each load condition tested. The error associated with each calibration was calculated using the goodness of fit (GOF) for each calibration curve assessed against all data points from all trials for all load conditions. For example, the calibration curve associated with the 5 mm × 5 mm occluder at 150 mm/s loading was evaluated using all data points from the 3 trials for each of the 4 load conditions (5 mm × 5 mm and 10 mm × 10 mm at either 2 mm/s or 150 mm/s). The error associated with each calibration curve was approximated using the standard error of the estimate

(S_{est}) [46] GOF statistic (Equation 3-5). The S_{est} is closely related to the sum of the squares error as it incorporates the sum of the squares of the differences between a predicted value and a measured value for each data point. These error differences are scaled according to the number of data points and degrees of freedom in the model, producing a representation of the standard deviation of the errors for the fit.

The S_{est} statistic was chosen because it produces a value that has the same units as that being predicted by the calibration curve, and is more readily applied to data fit with a non-linear curve than the more commonly reported R^2 value which is based off the assumption of a linear fit to data [47]. By calculating the standard error of the estimate for each calibration curve against all speed and occluder geometry load conditions, the error value produced encompassed the load rate and occluder geometry variability associated with the SCOT calibration.

$$S_{est} = \sqrt{\frac{\sum_i (Y_i - Y'_i)^2}{n - dof}}$$

Equation 3-5 Standard error of the estimate (where S_{est} = the standard error of the estimate, Y_i = ith data point, Y'_i = ith predicted data point, n = number of data points, and dof = number of degrees of freedom in the fitted model.

Curve fitting and assessment of the GOF statistics for each curve was repeated for each SCOT segment and results exported for further analysis. The calibration curve used for data collected during tests was that which had the smallest average S_{est} attributed to it. That is, the calibration curve that best described all calibration data points was used for subsequent tests.

3.3 Results

3.3.1 Static Calibration

The static calibration using the 10 mm × 10 mm occluder was performed to determine the limits of measureable TCA using the SCOT. The minimum measurable TCA using the SCOT was 107.6 ± 1.2 mm^2 (mean ± 1 standard deviation). An example trace of the TCA is presented in Figure 3-3. The 3rd order polynomial relationships between radial compression of the SCOT and TCA obtained prior to this work are presented in Table 3-1.

Table 3-1 : Summary of fits relating total cross-sectional area (TCA) to occlusion ratio (r, which is the ratio of radial compression to SCOT casing unoccluded outer diameter)

$$TCA = f(r) = ar^3 + br^2 + cr + d, where\ r = occlusion\ ratio = \frac{radial\ compression}{casing\ outer\ diameter}$$

Occluder	a [95% conf. int.]	b [95% conf. int.]	c [95% conf. int.]	d [95% conf. int.]	R^2
5 mm × 5 mm	256.9 [164.8,349.0]	-360.4 [-445.6,-275.2]	-8.9 [-30.0,12.2]	199.8 [198.3,201.3]	0.9997
10 mm × 10 mm	337.4 [98.4,576.4]	-466.0 [-693.2,-238.7]	-0.8 [-60.0,58.3]	200.7 [196.6,204.8]	0.9980

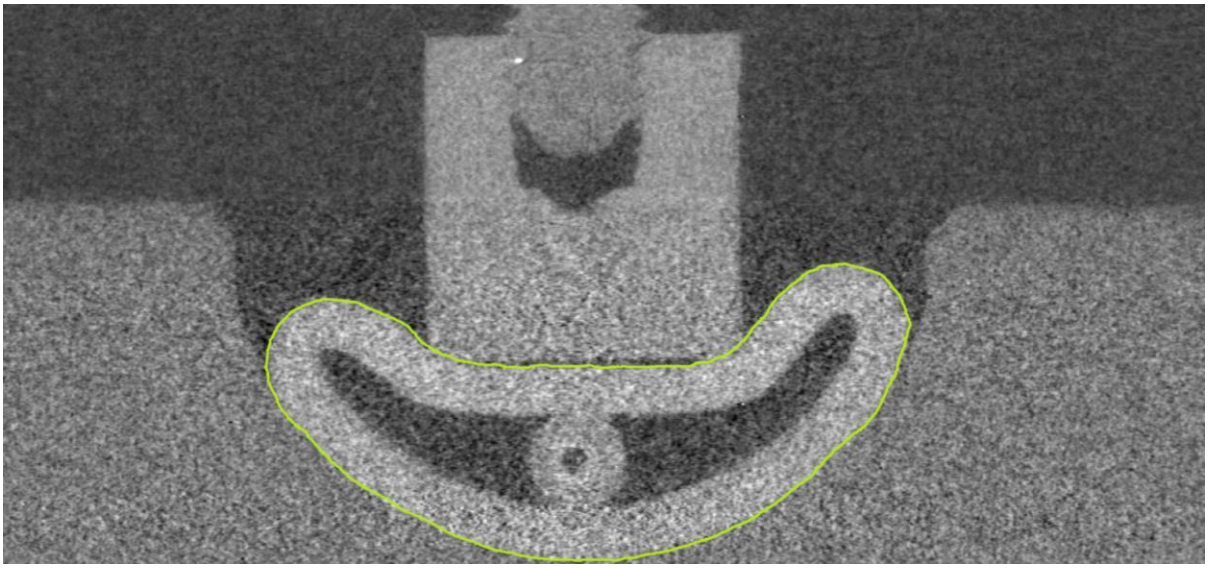

Figure 3-3 Example trace of TCA from CT scans of SCOT at maximum radial compression (NB. The green trace line has been made thicker to aid in visualization).

3.3.2 Dynamic Calibration

Dynamic calibrations were performed before testing each day as part of the flexibility study described in Chapter 4:. This resulted in a total of 8 dynamic calibrations (1 pilot and 7 specimens) over the course of 16 days. Table 3-2 presents example calibrations for a single SCOT segment from the beginning, middle and end of the study period. Figure 3-4 presents an

example of the 4 calibration curves produced for SCOT segment 5 on day 16 of testing, as well as all data points from all trials and calibration load conditions. This plot highlights the inability for a single calibration curve to describe all load conditions, and the necessity to use a GOF statistic such as S_{est} to identify the curve that results in the minimum discrepancy between fit and actual data. The Sest values for each calibration type averaged over all SCOT segments and all test days were 6.1 ± 1.4 mm^2, 10.9 ±1.5 mm^2, 5.0 ± 1.2 mm^2 and 5.3 ± 1.3 mm^2 for 5 mm × 5 mm at 2 mm/s, 5 mm × 5 mm at 150 mm/s, 10 mm × 10 mm at 2 mm/s and 10 mm × 10 mm at 150 mm/s, respectively. Finally, Figure 3-5 illustrates the variation of the calibration constant, a, for 5 mm × 5 mm and 10 mm × 10 mm occluder shapes at 150 mm/s, with respect to calibration day for SCOT segment 5.

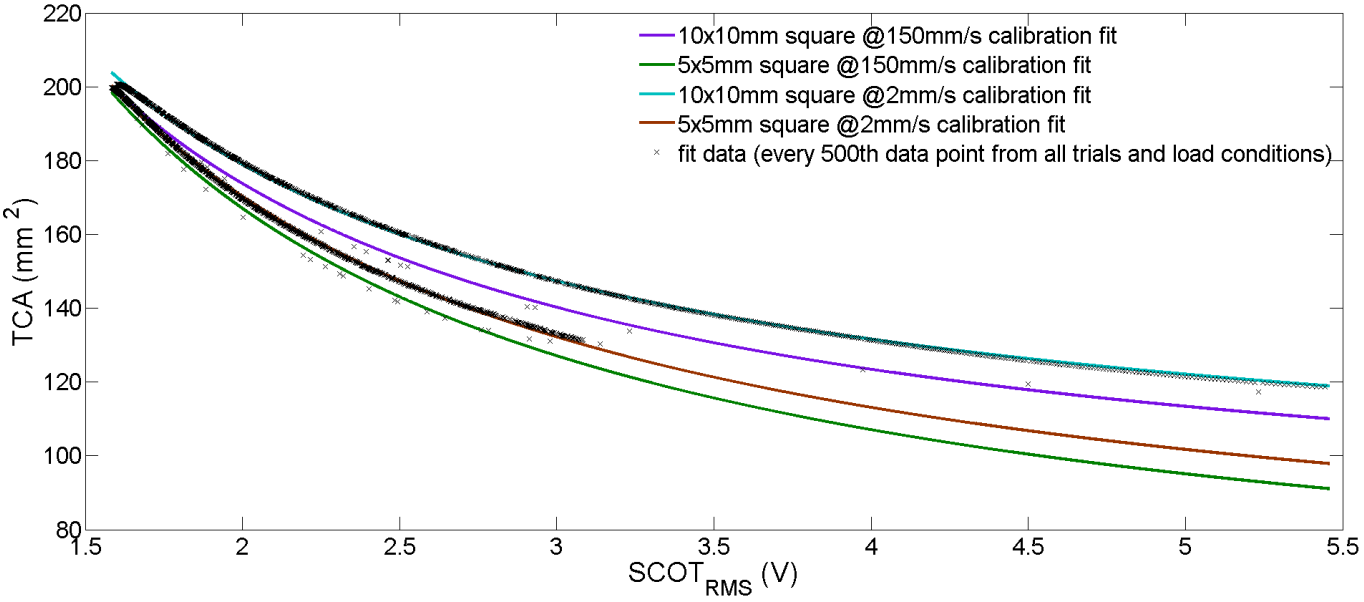

Figure 3-4 Example plot of the 4 calibrations curves produced for SCOT segment 5 and the data points from all load conditions and all trials on day 16 of testing.

Table 3-2 Example calibration results for SCOT segment 5 for two calibration load conditions over the course of a 16 day study period (where ($Y-Y_{fit}$) is the error for each data point in the fit; S_{est} is the standard error of the estimate; a and b are the averaged calibration fit constants for the 3 trials for each calibration load condition)

$$TCA = \frac{a}{SCOT_{RMS}} + b$$

Test day	Calibration Type	a (±1 SD)	b (±1 SD)	S_{est} (mm^2)	Mean ($Y-Y_{fit}$) (±1 SD) (mm^2)	R^2
6	5 mm × 5 mm @ 150 mm/s	246.1 (±0.9)	45.2 (±0.7)	10.1	8.5 (±5.3)	0.8462
	10 mm × 10 mm @ 150 mm/s	216.2 (±0.9)	64.5 (±0.7)	4.3	3.1 (±3.0)	0.9713
9	5 mm × 5 mm @ 150 mm/s	250.6 (±0.4)	38.5 (±0.3)	10.6	9.1 (±5.5)	0.7991
	10 mm × 10 mm @ 150 mm/s	214.3 (±2.6)	62.0 (±2.1)	4.4	3.4 (±2.7)	0.9660
16	5 mm × 5 mm @ 150 mm/s	239.8 (±0.4)	47.1 (±0.3	11.8	8.8 (±7.5)	0.7604
	10 mm × 10 mm @ 150 mm/s	201.1 (±0.2)	73.2 (±0.03)	5.2	1.3 (±5.0)	0.9520
Mean* **(±1 SD)**	5 mm × 5 mm @ 150 mm/s	246.8 (±6.4)	42.1 (±5.0)			
	10 mm × 10 mm @ 150 mm/s	211.5(±6.8)	65.1 (±4.9)			

* calculated for all calibrations conducted over the 16 test period

3.4 Discussion

3.4.1 Static Calibration

The static calibration from previous unpublished work conducted in our lab (Appendix A) was used to determine the relationships between TCA and depth of radial compression for both 5 mm × 5 mm and 10 mm × 10 mm occluder shapes. The change of design of the SCOT probe did, however, require a new static calibration to determine the minimum TCA possible before the SCOT casing was compressed into the sensing elements. This measurement was conducted and

the minimum TCA before compression of the SCOT probe was 107.6 ± 1.165 mm^2. Van Toen *et al* [36] reported a minimum measurable TCA of 99.5 mm^2 for the original SCOT. The reduced measurable range of TCA was expected due to the slightly increased diameter of the SCOT sensing elements when compared to the original design. The 8.14% reduction in measurable range was considered to be acceptable given the improvements in durability of the new design.

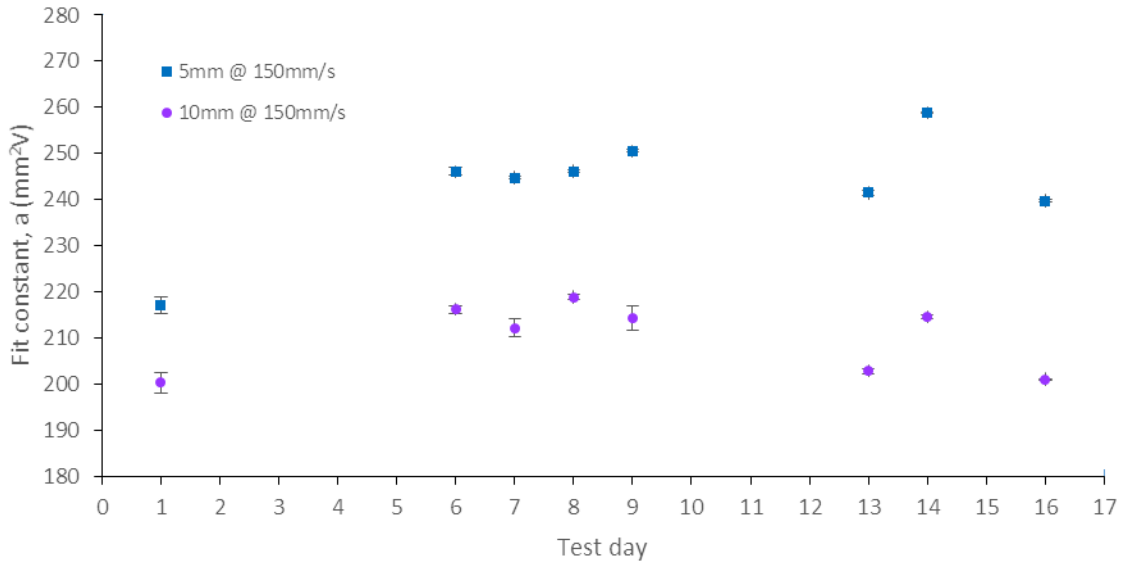

Figure 3-5 Variation of fit constant, a, with respect to test day for SCOT segment 5 for 5 mm × 5 mm and 10 mm × 10 mm occluder shapes at 150 mm/s calibration load conditions (error bars are ±1 standard deviation). NB. Only fit constant a is presented as it directly affects the relationship between radial compression and SCOT output. Fit constant b is just a zero load offset.

3.4.2 Dynamic Calibration

The dynamic calibration method was performed before each test throughout the flexibility study described in Chapter 4. By performing 8 dynamic calibrations over a 16 day study period, the variation of calibration with respect to time was identified. Figure 3-5 clearly shows that the

calibration constant changed throughout the study period. For the case of fit constant *a*, the standard deviation of *a* for all calibrations was calculated for each SCOT segment and normalized against the value for *a*. The maximum standard deviation was 3.8%, resulting in a deviation of TCA measurement between 2.2 mm^2 and 9.2 mm^2 depending on the SCOT output (since the SCOT calibration is non-linear, the deviation is larger at lower SCOT outputs).

Possible causes of variations of the calibration curves with time include the degradation or improper mixing of the conductive saline solution used to fill the SCOT casing, slight variations in the way the SCOT probe was positioned within the SCOT casing, and inconsistencies in the positioning of the occluder against the SCOT casing prior to loading. Efforts were made to reduce variability associated with the conductive saline by using the same small batch mixed prior to the beginning of the flexibility study (Chapter 4:), and by thoroughly mixing the saline before use. We used a specially designed plug and sponge to reduce variation in resultant SCOT signals due to movement of the SCOT probe within the casing. Though the movement of the probe was limited by these components, it was not completely removed and the probe was still able to move slightly within the SCOT casing, likely contributing to the variations in calibration presented. Finally, though every effort was made to ensure the occluder was in contact with, but without causing radial compression of the SCOT casing, this was impossible to guarantee. Any variation in the unoccluded, 0 mm radial displacement condition for each calibration curve would result in inconsistent SCOT outputs for given radial displacements. This was likely the largest contributor to calibration variation, though it is unclear how this could be addressed. Attempts were made to determine first contact with the SCOT casing by monitoring the load

applied by the occluder; however, the sensitivity of the load cell available for initial pilot tests was too low and this method was not employed for calibrations during the flexibility study.

A new method for describing the error associated with SCOT measurements of TCA using the standard error of the estimate has been described. The S_{est} was chosen to describe the error associated with the SCOT calibrations as it shared the same units as the TCA that was being measured using the calibrations, and is more readily applied for non-linear curve fitting. The calibration using the 10 mm × 10 mm occluder typically resulted in the minimum S_{est} when compared with all data points from all calibration load conditions. Since the intended use of the SCOT was for impact studies at load rates up to 500 mm/s, the decision was made to use the 10 mm × 10 mm at 150 mm/s load condition calibration curve. The calibration error was calculated for each test day, with the mean error over all test days 5.3 ± 1.3 mm^2. The 10 mm × 10 mm at 150 mm/s load condition also produced the most consistent calibrations, with the standard deviation for both fit constants smaller than for other calibration load conditions.

Chapter 4: Measurement of Spinal Canal Occlusion During Non-Pathological Bending of Cervical Spine Segments

4.1 Introduction

The purpose of this study was to investigate the response of the newly designed SCOT when used in long cervical spine segments during non-injurious, continuous bending. To meet this aim, the hypothesis that non-injurious bending of the cervical spine will not result in changes in total canal area that exceed the error associated with the SCOT was tested.

4.2 Materials and Methods

4.2.1 Specimen Preparation

Seven fresh-frozen cadaveric cervical spines (four C2-C7, two C4-T2 and one C3-T1) were procured and stored at -20 ˚C until use. Specimens were dissected free from musculature, keeping the ligaments and IVDs intact. The spinal cord was removed from the specimens and replaced with a length of flexible tubing with outside diameter 15.9 mm (Tygon R-1000, Norton Performance Plastics, Canton, OH) used by the SCOT. The superior and inferior vertebrae of each segment were potted in dental stone (Modern Materials Tru-Stone Pink, Heraeus Kulzer GmbH, IN, U.S.A.) with the SCOT tubing extending through the potting. Segments were aligned such that the middle IVD of the segment was parallel with the loading attachments and the natural curvature of each spine was maintained. A summary of the specimen and donor details are presented in Table 4-1.

Table 4-1 Summary of specimen and donor details for this study

Specimen number	Age, gender	Level	Notes
H1006	79, F	C2-7	
H1007	83, M	C2-7	C34 left facet capsule disrupted
H1010	84, M	C3-T1	T1 fracture
H1012	62, M	C2-7	
H1019	85, M	C4-T2	
H1021	90, M	C2-7	
H1029	90, F	C4-T2	
Mean (std.)	81.9 (9.6)		

4.2.2 Loading

Specimens were subject to three-dimensional flexibility testing (Figure 4-1). Non-constraining continuous bending moments were applied to the superior vertebra up to 4 Nm in flexion-extension, left and right axial rotation, and left and right lateral bending, at a rate of 2 ˚/s [48]. Flexion-extension and lateral bending loads were chosen to match those employed by Nuckley *et al*[12] (4 Nm flexion-extension and left-right lateral bending). A larger, 4 Nm load in axial rotation compared to 3 Nm applied by Nuckley *et al* [12] was used in an effort to observe any responses from the SCOT at maximal, non-pathological rotation. Specimens were observed by three lab members to identify any possible injuries during the load protocol. Three loading cycles were applied in each direction, and the third cycle was used for analysis.

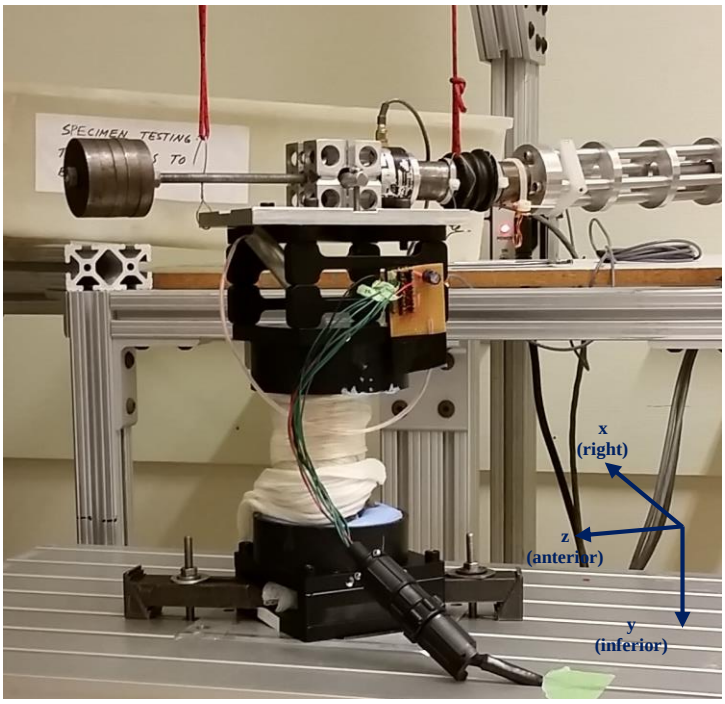

Figure 4-1 Experimental setup illustrating a lateral view of a C2-C7 spinal segment. Approximate orientation of the anatomic coordinate system is illustrated in the inset. NB This image is of the pilot specimen which used PMMA instead of dental stone for potting

4.2.3 Instrumentation and Data Acquisition

A custom LabVIEW program (National Instruments, Austin, TX) was used to collect torque outputs from a torque measuring load cell (TRT-200, Transducer Techniques, Temecula, CA) and angle displacement outputs from the servo motor applying the loads (D50R10-0243, Designatronics, New Hyde Park, NY) at a rate of 20 Hz.

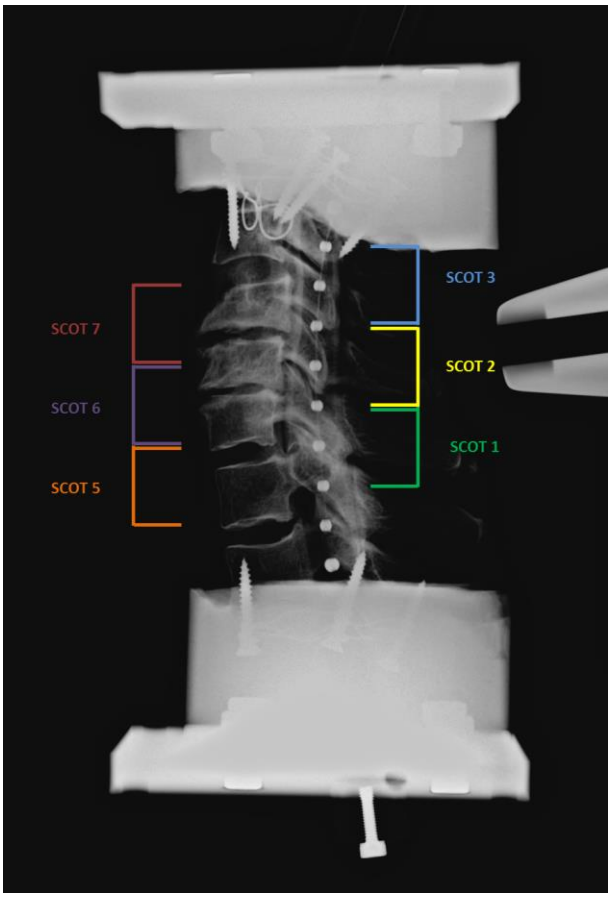

Figure 4-2 : Example lateral x-ray of specimen H1029 potted with SCOT probe in place. Each measurement segment is labelled

The SCOT was calibrated before potting the specimen each test day following the methods outlined in Chapter 3:. The SCOT tube used during potting was replaced with a clean tube and

inserted into the specimen so that it extended a short distance beyond the inferior potting. The SCOT probe was passed through the tubing in the canal and inserted into a plug that was then used to seal the inferior end of the tube. Spacers in the plug were used to ensure the measurement segments of the SCOT probe spanned the entire motion segment; this was confirmed using lateral plane x-ray (Figure 4-2). The specimen, with SCOT in place, was then fixed to the spine loading machine for testing. Once in place, the SCOT tube was filled with conducting fluid (0.9% wt. saline). SCOT input signal, SCOT segment output signals, and torque output signal were collected using a custom LabVIEW program (National Instruments, Austin, TX) and modular high speed DAQ system (cDAQ 9172 with NI 9215 modules, National Instruments, Austin, TX) at a rate of 50 kHz.

4.2.4 Data Analysis

Custom MATLAB code (version 7.13.0.564, MathWorks Inc., Natick, MA) was used for all data analysis. SCOT data collected on the high speed DAQ was aligned with data collected by the spine machine using the torque output data (collected using both systems). Peak moments from all three load cycles were identified in each data set and the mean delay between peaks calculated. The mean delay was then used to align data sets. Once data sets were aligned, torque data was zeroed and low-pass filtered (second order, Butterworth, 100 Hz cut off). Raw SCOT outputs were low-pass filtered to remove direct current offset (second order, Butterworth, 120 Hz cut off) and then converted to minimum transverse cross-sectional areas using the calibrations performed before testing. Percent changes in TCA (% dTCA) for each segment were normalized using the following equation:

$$SCOT\ \%\ dTCA(t) = (A(t) - A_0)/(A_0) \times 100$$

Equation 4-1 Equation for percent change in TCA (where $A(t)$ is the minimum outside area of the tube at time t, and A_0 is the initial minimum outside area prior to specimen loading)

Maximum decreases in TCA (maximum$(-1 \times SCOT\ \%dTCA)$) and the corresponding angle displacement and torque applied were identified for each loading direction (left and right axial rotation, left and right lateral bending, and flexion and extension) in each test. Maximum decrease in TCA were compared between pairs of bending directions using a paired t-test (dof=7, significance level set at $p<0.05$). Total ROM, defined as the sum of flexion and extension, left and right axial rotation, and left and right lateral bending angle displacements were calculated for each specimen (Table 4-2) and compared with previously reported equivalent segment total ROM (Table 4-4 and Table 4-5).

4.3 Results

No specimen injuries were observed during flexibility testing. Examples of applied torque and resultant TCA versus time plots are presented in Figure 4-3. The locations maximum decreases in TCA are presented in Figure 4-4 for all specimens.

Mean maximum percent decreases in TCA were 5.8%, 15.9%, 5.1%, 4.6%, 4.6% and 4.2% for flexion, extension, left axial rotation, right axial rotation, left lateral bending, and right lateral bending, respectively (Table 4-3). Of all bending directions considered, only extension consistently demonstrated mean maximum decreases that exceeded the mean error

(5.3±1.3 mm^2) as defined in Chapter 3:. When considering the effect of loading direction on maximum decrease in TCA, only flexion-extension loading demonstrated significant differences (*p=0.002*).

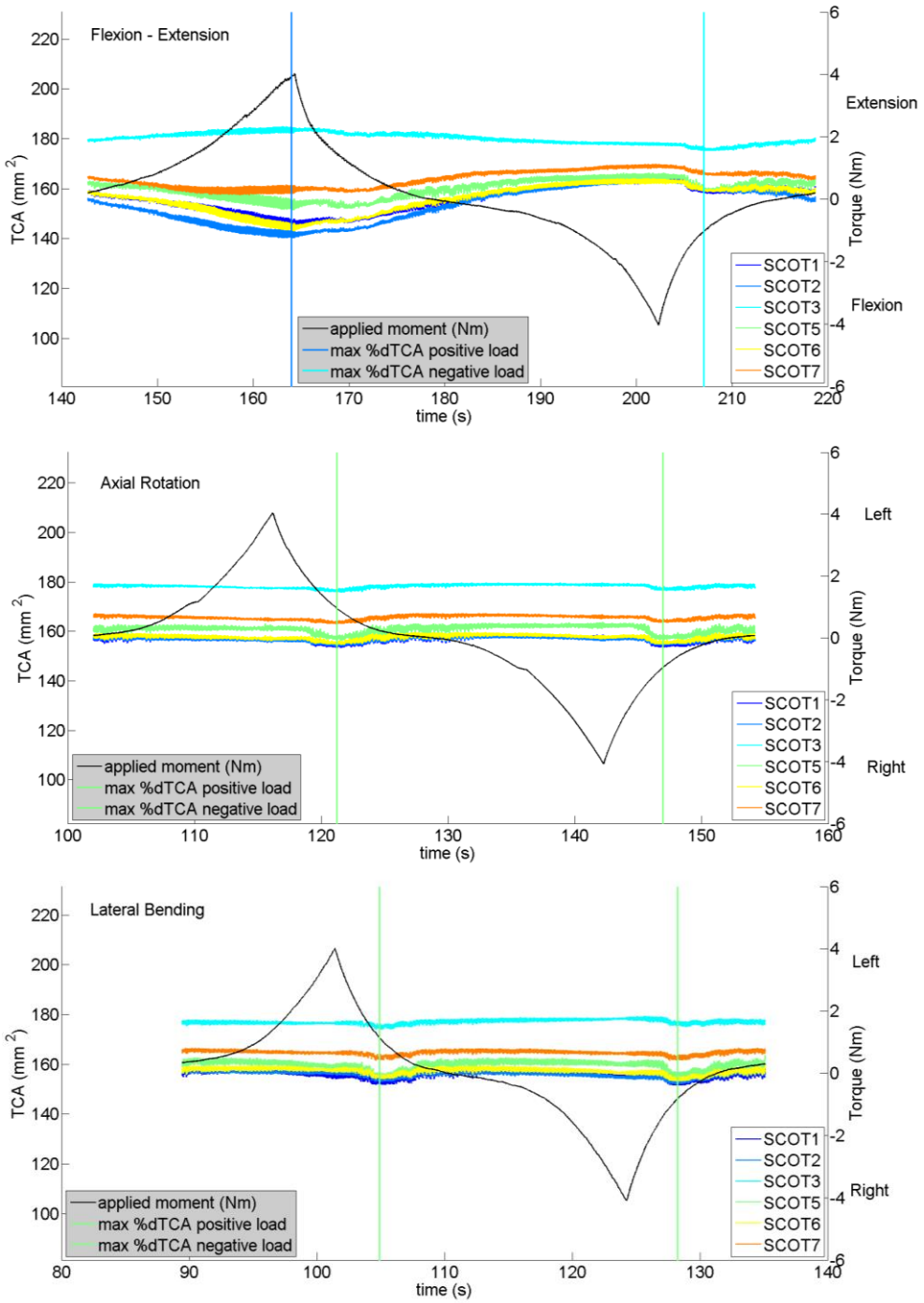

Figure 4-3 Typical plots (specimen 1029) of TCA and applied torque versus time for flexion-extension (top), left-right axial rotation (middle), and left-right lateral bending (bottom). Vertical lines represent times when maximum % decrease in TCA occurred; colors of vertical lines represent the SCOT segment that experienced the decrease.

Table 4-2 Summary of total ROM for flexion-extension, left-right axial rotation, and left-right lateral bending for the present study and expected total ROM from previously reported literature [49-55].

Specimen	Level	Flexion-extension			Axial rotation			Lateral bending		
		Present Study	*Expected in vivo*	*Expected in vitro***	*Present Study*	*Expected in vivo*	*Expected in vitro***	*Present Study*	*Expected in vivo*	*Expected in vitro***
H1006	C27	68.45	67.2	41.0	58.23	35.0	23.1	50.79	30.0	39.8
H1007	C27	87.37*	67.2	41.0	93.85*	35.0	23.1	64.29*	30.0	39.8
H1010	C3T1	76.59	72.0	41.9	60.11	32.0	22.8	52.17	30.0	35.7
H1012	C27	77.58	67.2	41.0	68.65	35.0	23.1	63.89	30.0	39.8
H1019	C4T2	68.45	62.4	38.1	62.19	27.4	20.1	44.53	26.8	29.4
H1021	C27	47.82	67.2	41.0	37.89	35.0	23.1	27.86	30.0	39.8
H1029	C4T2	75.30	62.4	38.1	51.68	27.4	20.1	45.23	26.8	29.4

**H1007 was noted to have a disrupted C3-4 facet capsule prior to the beginning of this study (Table 4-1)*
*** Expected in vitro ROM obtained under loads ranging from 0.07 Nm to 2.20 Nm*

Table 4-3 Summary of maximum percent decrease in TCA for each specimen in each bending direction. Included is the mean SCOT segment calibration error determined from each test day calibration as described in Chapter 3:.

Specimen number	Flexion (%)	Extension (%)	Left axial rotation (%)	Right axial rotation (%)	Left lateral bending (%)	Right lateral bending (%)	Calibration error (%)
H1006	5.2	12.1	5.5	4.7	5.1	3.3	5.5
H1007	6.2	32.4	14.8	6.3	6.0	6.1	6.2
H1010	7.3	22.2	5.0	4.6	3.3	3.4	5.4
H1012	8.0	19.9	7.3	6.3	7.0	6.4	5.2
H1019	6.51	11.1	5.3	5.5	5.7	5.4	5.0
H1021	5.6	19.9	4.3	4.2	3.2	3.4	5.2
H1029	2.3	10.0	2.8	2.6	3.4	3.1	6.0
**Mean (std.)*	5.8 (2.0)	15.9 (5.4)	5.1 (1.5)	4.6 (1.2)	4.6 (1.6)	4.2 (1.4)	

*H1007 removed from mean and standard deviation calculation due to compromised C3-4 facet capsule noted in Table 4-1

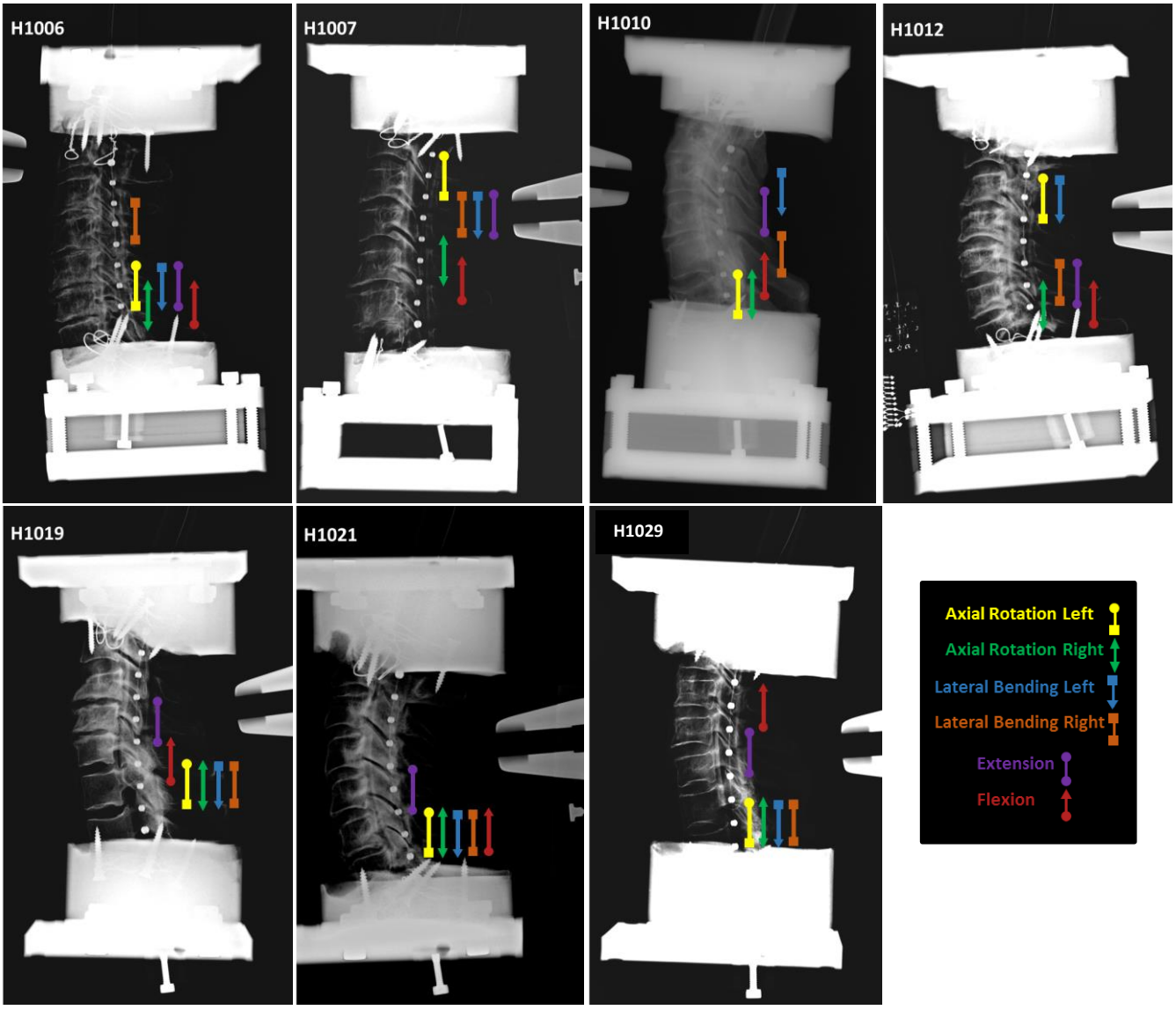

Figure 4-4 Lateral x-rays of each specimen with segments that experienced maximum decrease in TCA highlighted for each bending direction. NB. Caliper distance is set to 10 mm in each image

4.4 Discussion

4.4.1 ROM

The varying segment lengths for each specimen made comparison with published literature difficult. Total ROM for each segment was compared with the sum of individual segment ROM

reported in both *in vivo* (Table 4-4) and *in vitro* (Table 4-5) research. No literature was identified that reported C7-T1 ROM for either *in vivo* or *in vitro* studies, so predicted ROM for comparison with the present study was taken to be the same as the C67 ROM in each bending direction. Furthermore, no data describing *in vitro* ROM for T1-2 motion segments were identified, so these were taken to be the same as *in vivo* measurements. A comparison of previously reported total ROM and observed total ROM for each specimen is presented in Table 4-2. All specimens were observed to have a much larger total ROM compared to total ROM from *in vitro* studies. When compared to *in vivo* studies, specimens were observed to undergo a much larger total ROM for left-right axial rotation and left-right lateral bending; however, these differences were not as pronounced for total ROM in flexion-extension.

One contributor to total ROM discrepancies may be the age of the donors from which the specimens in the present study were procured. It has been established previously that the biomechanical properties of spinal ligaments deteriorate with age [56, 57]. The mean age of donors for this study was 81.9 years, whereas the mean age for donors in the papers referenced for comparison ranged from 22.6 years to 55.4 years [49-55]. Furthermore, the applied loads in previous studies were small, ranging from 0.07 Nm to 1.12 Nm, whereas the ROM considered in the present study was at 4 Nm. Deterioration of the spinal ligaments in the form of reduced stiffness would have facilitated an increased total ROM, particularly when subjected to the larger, 4 Nm loads applied in all bending directions used in this study.

The application of continuous bending moments in the present study may also have contributed to the discrepancies in total ROM. The studies referenced for comparison employed a stepwise

loading method; however, it has been reported previously that the neutral zone and ROM of cervical spine segments is increased when using stepwise loading when compared to continuous loading [48].

Nuckley *et al* [12] applied similar loads to those used in the present study to specimens with a mean donor age of 74 years; however only total ROM for the C4-C6 segment were reported. The authors described the observed 29.6 ± 6.5 ˚, 18.6 ± 7.4 ˚ and 15.9 ± 4.7 ˚ for flexion-extension, lateral bending and axial rotation, respectively, as *"Physiologic intact cervical range of motion across C4-C6".* If the total ROM of the sub-atlanto cervical spine were considered to be evenly distributed across each motion segment from C2-C7, then the predicted total ROM from the Nuckley *et al* [12] study would be 74.0 ˚, 46.5 ˚, and 39.8 ˚ for flexion-extension, lateral bending and axial rotation, respectively. In comparison, the mean total ROM observed in C2-C7 segments from this study (excluding the damaged H1007 specimen) were 70.6 ± 17.3 ˚ for flexion-extension, 47.5 ± 18.2 ˚ for lateral bending, and 54.9 ± 15.6 ˚ for axial rotation. Since both the age of the specimens and the bending loads applied to them were comparable with the present study, this offers a possible insight into how the effects of the age of the specimens combined with the larger bending loads may have influenced the larger total ROM observed in the present study, compared to the previously reported literature [49-55].

Furthermore, since the completion of this study, a second study comparing the ROM identified by the spine machine encoder and the ROM measured using Optotrak (Optotrak Certus, Northern Digital Inc., Waterloo, ON) markers placed on a dummy specimen has been performed (Appendix E). This study showed that the actual motion of the dummy specimen deviated from

the recorded motion from the encoder by up to 27%. The large differences were attributed to out of plane motion of the specimen and backlash experienced at the U-joints used in the spine machine design. Since the previously reported studies used methods with a more accurate measurements of spinal motion, it is likely that inconsistencies in observed ROM in the present study are at least partially due to this error. Optotrak markers could have been included on the upper and lower potting of the specimen to track the total segment ROM more accurately; however, this was not the main objective of the study and it was hoped that the encoder data would suffice.

Table 4-4 : *In vivo* studies reporting lower cervical spine segmental total ROM (in degrees) in flexion-extension, left-right axial rotation, and left-right lateral bending

Author	C23	C34	C45	C56	C67	C7T1	T1T2	Notes
Flexion-extension								
Penning **[52]**	12	18	20	20	15	-	-	*20 healthy young adults*
Dvorak *et al* **[58]**	10	15	19	20	19	-	-	*28 healthy adults*
Lind *et al* **[59]**	10 (4)	14 (6)	16 (6)	15 (8)	11 (7)	-	-	*70 subjects, age 12-79 years*
Dvorak *et al* **[60]**	12	17.2	21.1	22.6	21.4	-	-	
Holmes *et al* **[51]**	7.7	13.5	17.9	15.6	12.5	-	-	*50 subjects, mean age 47 years*
Morita *et al* **[50]**	-	-	-	-	-	-	3.9 (2.8)	*50 subjects, mean age 55.4 years*
Axial rotation								
Dvorak *et al* **[61]**	6	13	13.4	14	10.8	-	-	*9 subjects, mean age 30 years*
Penning **[62]**	6	13	13.6	13.8	10.8	-	-	*26 subjects, mean age 22.6 years*
Mimura *et al* **[63]**	7.4	5.8	4.2	5.4	6.4	-	-	*20 subjects, mean age 27.1 years*
Iai *et al* **[55]**	9	7	7	6	6	-	-	*20 subjects, mean age 27.7 years*
Fujimori *et al* **[54]**	-	-	-	-	-	-	2.4*	*13 subjects, mean age 33.2 years*
Lateral bending								
Penning **[52]**	6	6	6	6	6	-	-	*20 healthy young adults*
Fujimori *et al* **[53]**	-	-	-	-	-	-	2.8*	*15 subjects, mean age 32.8 years*

**Mean of left and right motions was doubled to obtain total ROM as defined in this table*

Table 4-5 *In vitro* studies reporting segmental lower cervical spine total ROM (in degrees) in flexion-extension, left-right axial rotation, and left-right lateral bending

Author	Load	C23	C34	C45	C56	C67	C7T1	T12	Notes
Flexion-extension									
Moroney *et al* [64]	1.2-2.2 Nm	9.7	9.7	9.7	9.7	9.7	-	-	*Average value from 35 2-vertebrae FSUs from lower cervical spine*
Holmes *et al* [43]	0.07-0.12 Nm	4.8 (1.2)	7.7 (1.8)	9.4 (2.4)	11 (2.8)	10.2 (4.1)	-	-	*10 specimens, mean age 26 years*
Panjabi *et al* [49]	1 Nm	6.2	7.7	10.1	9.9	7.1	-	-	*16 specimens*
Axial rotation									
Lysell [65]	-	6	9.8	10.3	8	5.7	-	-	*28 specimens, mean age 52 years*
Moroney *et al* [64]	1.2-2.2 Nm	3.7	3.7	3.7	3.7	3.7	-	-	*Average value from 35 2-vertebrae FSUs from lower cervical spine*
Panjabi *et al* [49]	1 Nm	3.2	5.1	6.8	5.1	2.9	-	-	*16 specimens*
Lateral bending									
Moroney *et al* [64]	1.2-2.2 Nm	9.4	9.4	9.4	9.4	9.4	-	-	*Average value from 35 2-vertebrae FSUs from lower cervical spine*
Panjabi *et al* [49]	1 Nm	9.5	9.1	9.3	6.5	5.4	-	-	*16 specimens*

4.4.2 Spinal Canal TCA

Maximum decreases in TCA that exceeded the calibration error of the SCOT were identified in extension loading of the cervical spine. Since no injury to the ligamentous or osseous structures of the specimens were observed, the hypothesis that non-injurious loading of the cervical spine will not result in changes in total canal area that exceed the error associated with the SCOT is rejected.

The more pronounced maximum decreases in TCA observed in extension bending is in line with clinical observations of central cord syndrome (CCS), which is the most common form of incomplete SCI amongst the elderly population [66]. The etiology of CCS is typically a hyperextension injury to the neck combined with a pre-existing narrowing of the spinal canal, such as disc space collapse, development of osteophytes, ossification of the posterior longitudinal ligament, or hypertrophy of the ligamentum flavum [66-69]. The decreases in TCA observed in the present study illustrate the extent to which hyperextension of the neck, without disruption of the vertebral column, can cause a measurable occlusion of the cervical spinal canal.

Direct, quantitative comparison of the occlusions observed in the present study is made difficult due to the variability in segment length of specimens. Instead, we qualitatively described the occlusions each specimen experienced by visualizing the location of maximum decreases in TCA superimposed on x-rays of each specimen (Figure 4-4). Only flexion-extension bending directions produced occlusions that exceeded the SCOT calibration error; however, a closer examination of the occlusions that occurred did not highlight any trends. In fact, there is no obvious pattern in the location of the maximum decreases in TCA for any of the bending

directions considered. In five of the specimens, the maximum decrease in TCA for at least four of the six bending directions considered, occurred in overlapping SCOT segments. This may be indicative of a pre-existing condition that resulted in a narrowing of the spinal canal in the region.

Using the SCOT for measurement of the TCA has limitations. Though the SCOT tube consistently filled the spinal canal sagittally, it did not fill the canal laterally for all specimens. This will have resulted in an underestimate of TCA, and possibly an underestimate in maximum decrease in TCA during bending. Van Toen *et al* [36] noted that the spinal cord occupies only the middle third of the subaxial cervical spine mediolaterally, and the likelihood of occlusions in the lateral most space are of less clinical interest. Rather, the far lateral compression would manifest in the form of radiculopathy (single nerve root injury).

Another functional limitation of the SCOT in the present study is the segment length. The calibration characterized the minimum cross-sectional area of the SCOT tube over the entire 20 mm segment; however, this does not describe the exact location of the maximum occlusion. When Raynak *et al* [13] reported their development of the SCOT for use in their studies, the authors highlighted that despite this limitation, since minimum cross-sectional area is the most clinically relevant, the SCOT is still capable of illustrating significant dynamic changes in TCA.

4.4.3 Summary

In the present study, we investigated changes in TCA of lower cervical spine specimens when tested in flexion-extension, left-right axial rotation, and left-right lateral bending under normal

physiologic loads. Measureable reductions in TCA were observed in all bending directions; however, only bending in extension produced maximal decreases in TCA that exceeded the SCOT calibration error. Thus, the hypothesis that non-injurious loading of the cervical spine will not result in changes in total canal area that exceed the error associated with the SCOT was tested is rejected. Extension bending resulted in the largest decreases in TCA for all specimens. Whether these levels of occlusion could be responsible for SCI remains unclear since it is possible *in vivo* the spinal cord could move within the spinal canal to accommodate such a change in geometry. Nonetheless, the decrease in TCA observed only during extension bending illustrates the possible biomechanical mechanism responsible for CCS in a clinical setting.

Chapter 5: Discussion

5.1 Summary

The original SCOT designed by Raynak *et al* [13] and then later redesigned into a self-contained probe by Zhu *et al* [14] had suffered significant damage due to corrosion of sensing elements resulting in a compromised signal quality and inconsistent readings. These factors resulted in data loss during impact experiments investigating the effect of lateral eccentricity on the resultant injuries during dynamic axial compression of the cervical spine [36], necessitating a new SCOT probe design.

A new SCOT probe was built incorporating modifications to improve signal stability and probe durability. A total of six designs were prototyped and evaluated against the following design criteria:

1. The SCOT must continue to be usable with the existing electronics,
2. The SCOT must incorporate materials that can resist degradation due to corrosion, and
3. The SCOT should function with an SNR_{dB} and dV_{RMS} that matches or exceeds the performance of the original SCOT.

We considered modifying the geometry and materials of the sensing, excitation and ground elements, the sleeve material housing the SCOT probe wiring, and the type of electrical connection between sensing/excitation/ground elements and the wires that carried the signal. The six designs were tested using a standardised load protocol that closely matched the conditions used to calibrate previous iterations of the SCOT [13]. We tested the durability of the new

designs by repetitively loading the SCOT sensor at load rates up to 150 mm/s. We also assessed signal quality and consistency using static load holds during testing.

The results of the SCOT design process described in Chapter 2 facilitated the design and construction of a new SCOT probe that incorporated:

1. a more durable sleeve material and SS probe elements to improve corrosion and repeated impact resistance;
2. spherical probe elements to maximize the sensing surface area to ensure a strong signal ,
3. internally soldered electrical connections allowing complete sealing of the SCOT probe to reduce risk of water damage; and
4. the use of sponges and a specially designed plug to facilitate consistent locating of the SCOT probe in the centre of the SCOT casing.

The newly designed SCOT probe consisted of 3.97 mm diameter SS excitation and ground elements and 3.18 mm diameter SS sensing elements. A heat shrink sleeve was used to contain the 0.122 mm magnet wires that were soldered to the probe elements and then connected to the existing SCOT electronics. The design modifications of the SCOT probe have been tested repeatedly at load rates up to 2000 mm/s (Appendix D), demonstrating a substantially improved resistance to impact loading. Finally, the new SCOT probe operates using a 1.5 V_{pp} at 3 kHz input signal and has a 78.0 dB SNR, exceeding that of the original SCOT design.

The methods used to assess the different prototypes produced was not without its limitations. A more thorough repetitive loading protocol could have been utilized to assess the long term durability of each design. The failures due to waterproofing and impact resistance that occurred were identifiable soon into the testing protocol; however, long term durability of the chosen design remains unexamined. Furthermore, testing of the SCOT at speeds only up to 150 mm/s during these initial tests gave an incomplete view of both the signal response characteristics and the durability of the probe itself, particularly when its design intent was for experiments at higher energies.

The changes to the original SCOT probe design necessitated a new characterisation and calibration of the new SCOT probe design. A new static calibration was conducted to describe the minimum measurable TCA of the new SCOT probe. The results of this study highlighted an 8.14% increase in the minimum measurable TCA due to the slightly larger probe elements used; however, this reduction in measurable range (due to the increase in minimum measurable TCA) was deemed acceptable when weighed against the improvements in durability and signal stability.

Errors associated with dynamic calibrations of the new SCOT probe were assessed using the goodness of fit statistic, the standard error of the estimate (S_{est}). The S_{est} was chosen as it has the same units as the TCA that was calculated using the calibration curves, and is more readily applied to non-linear curve fits than the more typically reported R^2 coefficient. Calibration curves produced using the 10 mm × 10 mm occluder typically resulted in the minimum S_{est} when compared to all trials for all load conditions. Since the intended use of the SCOT was for impact

studies at load rates up to 500 mm/s, the decision was made to use the 10 mm × 10 mm at 150 mm/s load condition calibration curve. The 10 mm × 10 mm at 150 mm/s load condition also produced the most consistent calibrations, with the standard deviation for both fit constants smaller than for other calibration load conditions. Future dynamic calibrations should still be performed for all 4 load conditions presented in Chapter 3; however, curve fitting and analysis of error could be reduced to considering only the results of the 10 mm × 10 mm occluder at 150 mm/s load condition.

A total of 8 dynamic calibrations were performed over 16 days to assess the calibration consistency and error associated with the SCOT probe calibration. Variations in calibration with respect to time were observed over the 16 day study period and possible contributors to variation in the measured TCA identified. It is likely the most significant contribution to the variations in calibration over time was the 0 mm radial compression set point for each calibration trial. This variation could be minimized by using a more sensitive load cell to determine when contact between the occluder and SCOT casing first occurs. In the event this is not possible, more calibrations could be performed over another test period and the curves produced from these tests be combined with the existing curves to determine an average calibration curve for each calibration load condition. The results from such a study could be used to determine an overall calibration curve for the SCOT probe, with error estimates incorporating all trials over all test days. This would likely increase the error estimate, due to variation over all trials, but would no longer necessitate the calibration of the probe every day before testing.

The purpose of the study described in Chapter 4 was to demonstrate the functionality of the new SCOT probe in a cadaveric study of long cervical spine segments under non-pathological, continuous bending. This aim was achieved by testing the hypothesis that non-injurious loading of the cervical spine will not result in changes in total canal area that exceed the error associated with the SCOT. The largest decreases in TCA were highlighted in this study during extension bending (15.98% mean decrease in TCA) despite no evidence of disruption to the spinal column or surrounding soft tissue anatomy. Consequently, the hypothesis was rejected and a possible link to clinical occurrences of canal occlusion during extension bending such as central cord syndrome was identified. Whether the occlusions observed during extension could result in SCI remains unclear since it is possible *in vivo* the spinal cord could move within the spinal canal to accommodate such a change in geometry.

The use of the SCOT sensor in cadaveric studies has limitations. In particular, the inability for the SCOT casing to fill the cervical spinal canal laterally was highlighted. This limitation has been discussed previously by Van Toen *et al* [36] and it was posited that since the spinal cord only occupies the middle third of the subaxial spine mediolaterally, occlusions in the lateral most space of the spinal canal are of less clinical importance. Another limitation of the SCOT is the 20 mm segment length. The SCOT is calibrated for the minimum TCA over the entire 20 mm segment, thus limiting the ability to identify where the maximum occlusion of the canal occurred to somewhere within a 20 mm long region. Again, since the minimum TCA was considered to be of most clinical relevance when investigating the possibility of SCI [13], this was considered an acceptable limitation of the current SCOT probe design.

The most significant limitation of the flexibility study described in Chapter 4 was the ROM measurement. A study conducted after the completion of this flexibility study (Appendix E) highlighted significant differences between the ROM recorded by the apparatus used in the present study when compared to direct optoelectronic measurements of surrogate specimens. Previous flexibility studies conducted in our lab [36] have used an optoelectronic camera tracking system (Certus, Optotrak, Waterloo, ON, Canada); however, since the specimens used in this study were required for a different study, no disruption of any of the tissue was allowed. Time could have been taken to design and manufacture cradles that held the Optotrak markers without disrupting the specimens; however, since the purpose of this study was to confirm the usability of the new SCOT probe in cadaveric studies, specific ROM data for each test was not a priority. In hindsight, attaching a single Optotrak marker to the superior potting of the specimen would have allowed a more accurate measurement of total ROM throughout the flexibility study, and it is my recommendation that this become standard practice for all subsequent studies that require the specimen tissue remain without disruption.

5.2 Conclusions

The new SCOT has been constructed using corrosion resistant materials and tested at speeds up to 2000 mm/s without any indication of damage or compromised signal response. When considering the number of pilot studies, characterization trials, and the extensive calibrations conducted throughout the development, and later use of the SCOT in the flexibility study, the new SCOT has demonstrated corrosion resistance that exceeds that of the previous iteration (which showed signs of degradation after approximately 21 test days). The SNR of the new SCOT exceeds that of the original design when used with the same input conditions, and is

further improved when used with an increased input peak to peak voltage and frequency. Ultimately, the new design has been shown to be more durable, with an improved signal response when compared to the previous iteration that has been used in two previously published studies and a PhD dissertation [14, 15, 36]. With this in mind, there is no reason to not continue to use the new SCOT in the continuation of the work conducted by Van Toen *et al* [36, 70] in our lab, investigating the effects of lateral eccentricity on the response of the cervical spine under dynamic axial compression.

5.3 Future Work

Ideally, an update of the existing SCOT electronics hardware would be undertaken before any further use of the SCOT. The current electronics hardware is not shielded internally, and built using components that have likely degraded over the past approximately 20 years of use. Though the existing electronics were confirmed to still function as designed, an update of the electronics would likely improve signal noise and stability.

Bibliography

1. Davis, J.W., et al., *The etiology of missed cervical spine injuries.* J Trauma, 1993. **34**(3): p. 342-6.
2. Goldberg, W., et al., *Distribution and patterns of blunt traumatic cervical spine injury.* Annals of Emergency Medicine, 2001. **38**(1): p. 17-21.
3. Krueger, H., et al., *The economic burden of traumatic spinal cord injury in Canada.* Chronic diseases and injuries in Canada, 2013. **33**(3): p. 113-22.
4. NSCISC, *Annual statistical report - complete public version*, in *National Spinal Cord Injury Statistical Centre*. 2014, University of Alabama: Birmingham, AL.
5. DeVivo, M.J., et al., *Outcomes of post-spinal cord injury marriages.* Archives of Physical Medicine and Rehabilitation, 1995. **76**(2): p. 130-8.
6. Craig, A., Y. Tran, and J. Middleton, *Psychological morbidity and spinal cord injury: a systematic review.* Spinal Cord, 2009. **47**(2): p. 108-114.
7. Tate, D.G., et al., *Patterns of alcohol and substance use and abuse in persons with spinal cord injury: Risk factors and correlates1.* Archives of Physical Medicine and Rehabilitation, 2004. **85**(11): p. 1837-1847.
8. Panjabi, M.M., et al., *Multidirectional instabilities of traumatic cervical spine injuries in a porcine model.* Spine (Phila Pa 1976), 1989. **14**(10): p. 1111-5.
9. Panjabi, M.M.P., et al., *On the Understanding of Clinical Instability.* Spine, 1994. **19**(23): p. 2642-2650.
10. Panjabi, M.M., A.A. White Iii, and R.M. Johnson, *Cervical spine mechanics as a function of transection of components.* Journal of Biomechanics, 1975. **8**(5): p. 327-336.
11. Myers, B.S. and B.A. Winkelstein, *Epidemiology, Classification, Mechanism, and Tolerance of Human Cervical Spine Injuries.* 1995. **23**(5-6): p. 307-409.
12. Nuckley, D.J., et al., *Neural space integrity of the lower cervical spine: effect of normal range of motion.* Spine, 2002. **27**(6): p. 587-95.
13. Raynak, G.C., et al., *Transducers for dynamic measurement of spine neural-space occlusions.* Journal of Biomechanical Engineering, 1998. **120**(6): p. 787-791.
14. Zhu, Q., et al., *Translational constraint influences dynamic spinal canal occlusion of the thoracic spine: an in vitro experimental study.* Journal of Biomechanics, 2008. **41**(1): p. 171-9. Epub 2007 Aug 20.
15. Van Toen, C., *Biomechanics of cervical spine and spinal cord injury under combined axial compression and lateral bending loading*, in *Mechanical Engineering*. 2013, University of British Columbia: University of British Columbia.
16. Bogduk, N. and S. Mercer, *Biomechanics of the cervical spine. I: Normal kinematics.* Clinical Biomechanics, 2000. **15**(9): p. 633-648.
17. Moriya, H.M., et al., *Three-Dimensional Motion Analysis of the Cervical Spine with Special Reference to the Axial Rotation.* Spine, 1989. **14**(11): p. 1135-1139.
18. Gilroy, A.M., et al., *Atlas of anatomy*. 2nd ed. 2012, Stuttgart ; New York: Thieme. xv, 694 p.
19. Drake, R.L., et al., *Gray's anatomy for students*. 2nd ed. 2010, Philadelphia, PA: Churchill Livingstone/Elsevier. xxv, 1103 p.
20. Sekhon, L.H. and M.G. Fehlings, *Epidemiology, demographics, and pathophysiology of acute spinal cord injury.* Spine (Phila Pa 1976), 2001. **26**(24 Suppl): p. S2-12.

21. Dryden, D.M., et al., *The epidemiology of traumatic spinal cord injury in Alberta, Canada.* Canadian journal of neurological sciences, 2003. **30**(2): p. 113-21.
22. Lenehan, B.M.D.M.F., et al., *The Epidemiology of Traumatic Spinal Cord Injury in British Columbia, Canada.* Spine, 2012. **37**(4): p. 321-329.
23. El-Faramawy, A., et al., *Presentation and outcome of traumatic spinal fractures.* Journal of emergencies, trauma, and shock, 2012. **5**(4): p. 316-20.
24. Tator, C.H., et al., *Changes in epidemiology of acute spinal cord injury from 1947 to 1981.* Surgical Neurology, 1993. **40**(3): p. 207-15.
25. Jackson, A.B., et al., *A demographic profile of new traumatic spinal cord injuries: change and stability over 30 years.* Archives of Physical Medicine and Rehabilitation, 2004. **85**(11): p. 1740-8.
26. Pickett, G.E., et al., *Epidemiology of traumatic spinal cord injury in Canada.* Spine (Phila Pa 1976), 2006. **31**(7): p. 799-805.
27. Fredo, H.L., et al., *The epidemiology of traumatic cervical spine fractures: a prospective population study from Norway.* Scandinavian journal of trauma, resuscitation and emergency medicine, 2012. **20**(85): p. 85.
28. NSCISC, *Spinal Cord Injury Facts and Figures at a Glance.* Journal of Spinal Cord Medicine, 2015. **35**(6): p. 480-1.
29. Heinemann, A.W., B.D. Mamott, and S. Schnoll, *Substance use by persons with recent spinal cord injuries.* Rehabiltiation Psychology, 1990. **35**(4): p. 217-228.
30. Hartkopp, A., et al., *Suicide in a spinal cord injured population: its relation to functional status.* Archives of Physical Medicine and Rehabilitation, 1998. **79**(11): p. 1356-61.
31. Lee, B.B., et al., *The global map for traumatic spinal cord injury epidemiology: update 2011, global incidence rate.* Spinal Cord, 2013. **2013**(26): p. 158.
32. Chang, D.G., et al., *Geometric changes in the cervical spinal canal during impact.* Spine (Phila Pa 1976), 1994. **19**(8): p. 973-980.
33. Carter, J.W., et al., *Canal geometry changes associated with axial compressive cervical spine fracture.* Spine (Phila Pa 1976), 2000. **25**(1): p. 46-54.
34. Panjabi, M.M., et al., *Dynamic canal encroachment during thoracolumbar burst fractures.* Journal of Spinal Disorders, 1995. **8**(1): p. 39-48.
35. Carter, J.W., et al., *Tolerance of the cervical spine to eccentric axial compression*, in *Stapp Car Crash Journal*. 2002, SAE. p. 441-59.
36. Van Toen, C., et al., *The effect of lateral eccentricity on failure loads, kinematics, and canal occlusions of the cervical spine in axial loading.* Journal of Biomechanics, 2014. **47**(5): p. 1164-1172.
37. Saari, A., E. Itshayek, and P.A. Cripton, *Cervical spinal cord deformation during simulated head-first impact injuries.* Journal of Biomechanics, 2011. **44**(14): p. 2565-71.
38. Kroeker, S.G., et al., *The Development of an Improved Physical Surrogate Model of the Human Spinal Cord Tension and Transverse Compression.* Journal of Biomechanics, 2009. **42**(7): p. 878-83.
39. Bilston, L.E., D.F. Meaney, and L. Thibault. *The Development of a Physical Model to Measure Strain in a Surrogate Spinal Cord During Hyperflexion and Hyperextension*. in *International IRCOBI Conference on the Biomechanics of Impacts*. 1993. Eindhoven, Netherlands.

40. Pintar, F.A., et al., *Instrumented artificial spinal cord for human cervical pressure measurement.* Bio-Medical Materials and Engineering, 1996. **6**(3): p. 219-229.
41. Wilcox, R.K., et al., *A dynamic study of thoracolumbar burst fractures.* Journal of Bone and Joint Surgery American, 2003. **85-A**(11): p. 2184-9.
42. Wilcox, R.K., et al., *Measurement of canal occlusion during the thoracolumbar burst fracture process.* Journal of Biomechanics, 2002. **35**(3): p. 381-4.
43. Holmes, A.P., et al., *Changes in Cervical Canal Spinal Volume During In Vitro Flexion-Extension.* Spine, 1996. **21**(11): p. 1313-1319.
44. Dvorak, J., et al., *In vivo flexion/extension of the normal cervical spine.* J Orthop Res, 1991. **9**(6): p. 828-34.
45. Panjabi, M.P.D.T. and A.I.I.I.M.D.D.M.s. White, *Biomechanics of Nonacute Cervical Spinal Cord Trauma.* Spine, 1988. **13**(7): p. 838-842.
46. Pan, Q., *Standard Error of Estimate. Encyclopedia of Research Design. SAGE Publications, Inc*. Thousand Oaks, CA: SAGE Publications, Inc. 1425-1428.
47. Chung, M.K., *R2. Encyclopedia of Research Design. SAGE Publications, Inc*. Thousand Oaks, CA: SAGE Publications, Inc. 1188-1191.
48. Goertzen, D.J., C. Lane, and T.R. Oxland, *Neutral zone and range of motion in the spine are greater with stepwise loading than with a continuous loading protocol. An in vitro porcine investigation.* J Biomech, 2004. **37**(2): p. 257-61.
49. Panjabi, M.M., et al., *Mechanical properties of the human cervical spine as shown by three-dimensional load-displacement curves.* Spine, 2001. **26**(24): p. 2692-700.
50. Morita, D., et al., *Range of motion of thoracic spine in sagittal plane.* European Spine Journal, 2014. **23**(3): p. 673-678.
51. Holmes, A., et al., *The range and nature of flexion-extension motion in the cervical spine.* Spine (Phila Pa 1976), 1994. **19**(22): p. 2505-10.
52. Penning, L., *Normal movements of the cervical spine.* American Journal of Roentgenology, 1978. **130**(2): p. 317-326.
53. Fujimori, T., et al., *Kinematics of the thoracic spine in trunk lateral bending: in vivo three-dimensional analysis.* The Spine Journal, 2014. **14**(9): p. 1991-1999.
54. Fujimori, T.M.D.P., et al., *Kinematics of the Thoracic Spine in Trunk Rotation: In Vivo 3-Dimensional Analysis.* Spine, 2012. **37**(21): p. E1318-E1328.
55. Iai, H., et al., *Three-dimensional motion analysis of the upper cervical spine during axial rotation.* Spine (Phila Pa 1976), 1993. **18**(16): p. 2388-92.
56. Iida, T., et al., *Effects of aging and spinal degeneration on mechanical properties of lumbar supraspinous and interspinous ligaments.* Spine J, 2002. **2**(2): p. 95-100.
57. Cowin, S.C. and S.B. Doty, *Tissues Mechanics*. 2007, New York, NY, USA: Springer.
58. Dvorak, J.M., et al., *Functional Radiographic Diagnosis of the Cervical Spine: Flexion/Extension.* Spine, 1988. **13**(7): p. 748-755.
59. Lind, B., et al., *Normal range of motion of the cervical spine.* Arch Phys Med Rehabil, 1989. **70**(9): p. 692-5.
60. Dvorak, J., et al., *Clinical validation of functional flexion/extension radiographs of the cervical spine.* Spine (Phila Pa 1976), 1993. **18**(1): p. 120-7.
61. Dvorak, J., J. Hayek, and R. Zehnder, *CT-functional diagnostics of the rotatory instability of the upper cervical spine. Part 2. An evaluation on healthy adults and patients with suspected instability.* Spine (Phila Pa 1976), 1987. **12**(8): p. 726-31.

62. Penning, L. and J.T. Wilmink, *Rotation of the cervical spine. A CT study in normal subjects.* Spine (Phila Pa 1976), 1987. **12**(8): p. 732-8.
63. Mimura, M., et al., *Three-dimensional motion analysis of the cervical spine with special reference to the axial rotation.* Spine (Phila Pa 1976), 1989. **14**(11): p. 1135-9.
64. Moroney, S.P., et al., *Load-displacement properties of lower cervical spine motion segments.* J Biomech, 1988. **21**(9): p. 769-79.
65. Lysell, E., *Motion in the cervical spine. An experimental study on autopsy specimens.* Acta Orthop Scand, 1969: p. Suppl 123:1+.
66. Smith, S., T. Purzner, and M. Fehlings, *The Epidemiology of Geriatric Spinal Cord Injury.* Topics in Spinal Cord Injury Rehabilitation, 2010. **15**(3): p. 54-64.
67. Thompson, C., J. Gonsalves, and D. Welsh, *Hyperextension injury of the cervical spine with central cord syndrome.* European Spine Journal, 2015. **24**(1): p. 195-202.
68. Jabbour, P., et al., *Traumatic spine injuries in the geriatric population.* Neurosurgical Focus, 2008. **25**(5): p. E16.
69. Taylor, A.R., *THE MECHANISM OF INJURY TO THE SPINAL CORD IN THE NECK WITHOUT DAMAGE TO THE VERTEBRAL COLUMN.* Journal of Bone & Joint Surgery, British Volume, 1951. **33-B**(4): p. 543-547.
70. Van Toen, C., et al., *Cervical spine injuries and flexibilities following axial impact with lateral eccentricity.* European Spine Journal, 2015. **24**(1): p. 136-147.

Appendix A Previous Characterization of SCOT

The previous calibration of the SCOT was performed by Angela Melnyk in August 2013 for Dr. Peter Cripton and Dr. Tom Oxland. For further details, please contact one of these parties at:

Angela Melnyk

Tel. (604) 675-8827

Email. angela.melnyk@ubc.ca

Dr. Peter Cripton

Tel. (604)-822-6629 (at UBC main Campus)

Tel. (604)-675-8835 (at ICORD - VGH)

Fax. (604)-675-8849

Email. cripton@mech.ubc.ca

Dr. Tom Oxland

Tel. (604)-675-8834

Fax. (604)-675-8849

Email. toxland@icord.org

Appendix B Performance of Existing SCOT Electronics

B.1 Introduction

The electronic components of the SCOT system consist of a signal conditioning box and a constant current generator. These components are responsible generating a constant amplitude and frequency current (20 µA, 2 kHz sine wave) between the excitation and ground elements of the SCOT probe, and for measuring the difference in potential between adjacent (numbered) sensing elements. A voltage generator supplies the SCOT constant current generator with a constant amplitude and frequency input voltage (1 V_{pp}, 2 kHz sine wave) that drives it. Figure B-1 presents a flow chart illustrating the electronic components of the SCOT.

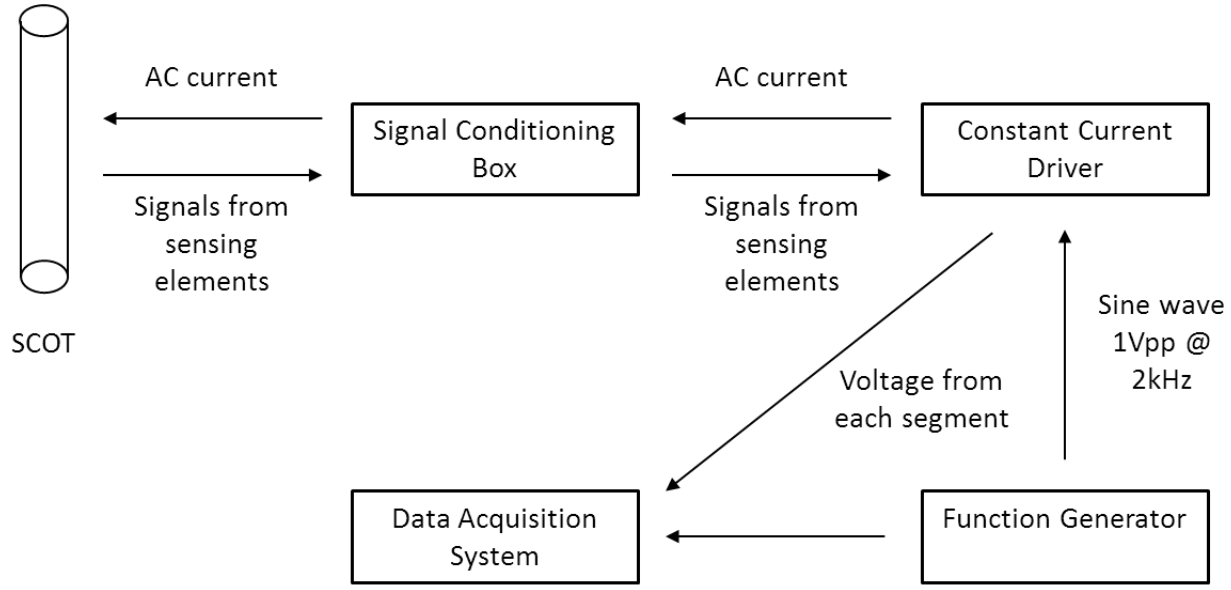

Figure B-1 Flow chart illustrating the electronic components of the SCOT

Both the constant current driver and signal conditioning box provide amplification to the voltage difference signals from each segment. The following appendix describes the work undertaken to confirm the existing SCOT electronic components continued to provide a constant current and

applied a constant gain for amplification of SCOT voltage signal. As an extension, the functionality of the constant current driver was investigated at higher input voltage amplitudes and frequencies.

B.2 Methods

A surrogate circuit was created to represent the SCOT probe using resistors in series. An additional resistor (R1) was then added to the surrogate SCOT probe circuit in parallel between adjacent sensing elements (Figure B-2).

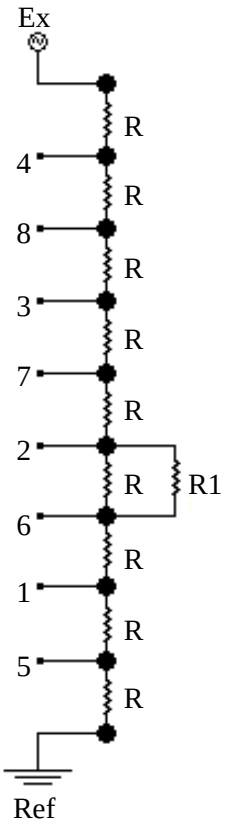

Figure B-2 Circuit diagram for surrogate SCOT probe used to assess the consistency of amplification gains and current produced by the existing SCOT electronics. NB. In this case, the additional resistor R1 is

connected so that SCOT segments 1 (2-1) and 6 (7-6) are loaded in addition to the constant loading supplied by resistors R = 33 Ω.

Amplification gains provided by the SCOT electronics were assessed by measuring the voltage across each segment at the surrogate circuit and at the SCOT output using an oscilloscope. Both the input voltage signal and values for R1 were varied to provide a range of loads for each SCOT segment. The values measured at the surrogate SCOT probe and the SCOT output were then used to calculate the amplification gain provided by the SCOT electronics.

Current supplied by the constant current divider was measured directly at the surrogate SCOT probe using a multimeter. The stability of the current provided by the constant current driver was assessed by varying the loading provided by R1, the input peak to peak voltage and the input frequency.

B.3 Results

Input voltage amplitudes in excess of 2.0 Vpp were observed to produce unloaded SCOT outputs beyond the range of the DAQ (±10 V) and were omitted from analysis. Table B-1 presents the mean measured gains for each SCOT segment for all loading and input signal conditions tested. Figure B-3 presents the current outputs from the constant driver for each signal input condition and loading applied (using R1).

Table B-1 Summary of amplification gains measured for all input signal and loading conditions

Input signal		Loading	Mean Gain (1 SD)*					
V_{pp}	**f (kHz)**	**R1 (Ω)**	**SCOT 1**	**SCOT 2**	**SCOT 3**	**SCOT 5**	**SCOT 6**	**SCOT 7**
1.0	2.0	0	506.7 (131.6)	538.7 9 (133.1)	511.1 (92.3)	647.1 (71.2)	646.3 (74.1)	653.6 (66.7)
2.0	2.0	0	557.1 (40.5)	562.2 (40.7)	537.4 (6.6)	565.4 (46.5)	545.1 (34.4)	548.0 (38.9)
2.0	3.0	0	534.1 (18.9)	540.6 (20.5)	537.3 (4.8)	541.1 (7.5)	536.0 (4.8)	536.0 (5.4)
2.0	4.0	0	541.3 (6.5)	544.1 (7.4)	538.3 (8.1)	545.6 (10.5)	548.4 (18.9)	547.7 (7.4)
2.0	2.0	200	553.8 (2.1)	555.9 (4.4)	548.8 (3.5)	551.9 (2.8)	553.7 (3.2)	551.7 (4.7)
2.0	3.0	200	550.5 (3.9)	553.7 (3.4)	550.3 (2.8)	554.5 (4.6)	552.5 (4.4)	553.1 (5.7)
2.0	4.0	200	550.4 (4.6)	553.8 (5.2)	549.7 (5.0)	552.0 (3.9)	552.9 (4.4)	552.6 (3.3)
2.0	2.0	268	548.2 (3.4)	548.6 (4.2)	547.6 (3.3)	547.3 (4.1)	550.3 (2.4)	548.4 (3.4)
2.0	3.0	268	546.0 (4.6)	549.4 (2.9)	548.9 (2.8)	547.0 (2.3)	548.1 (3.3)	547.4 (4.9)
2.0	3.0	268	549.7 (4.7)	549.5 (6.4)	547.5 (2.8)	547.9 (3.6)	549.4 (3.5)	547.9 (4.2)

** A total of 10 readings were taken for each input signal and loading condition. The mean and standard deviation were calculated using the sample of 10 trials*

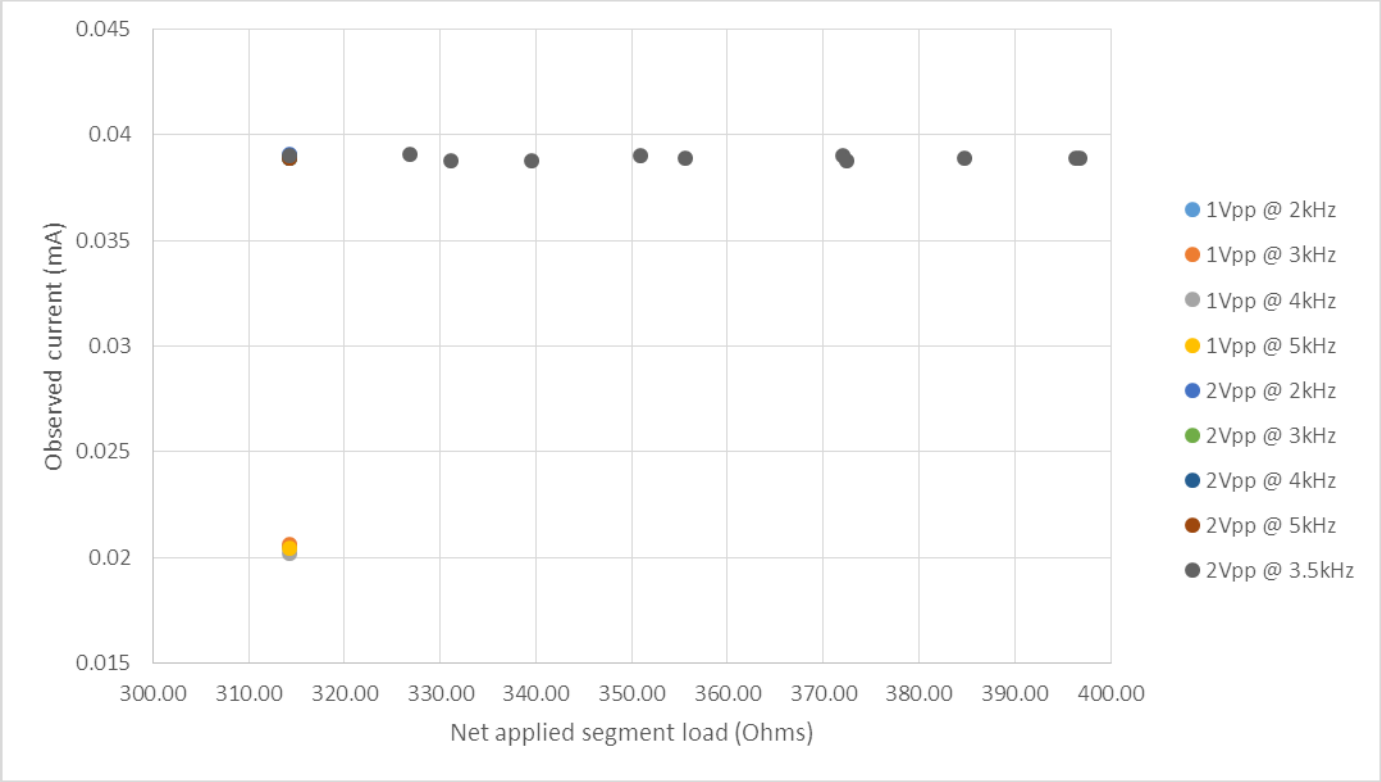

Figure B-3 Plot of observed current versus net applied loading using the surrogate SCOT probe. Each data point represents a single reading using a multimeter with error ±0.002 mA.

B.4 Discussion

By observing the standard deviations presented in Table B-1, it is evident that the stability of the gains produced by the SCOT electronics improved with an increasing input signal frequency and an increased loading on SCOT segments. The current output from the constant current driver was consistent (to within the 0.002 mA error of the multimeter used) across a range of input signal conditions and SCOT segment loading.

This study was not intended to be a thorough examination or characterization of the existing SCOT electronics; only a brief qualitative understanding was sought. The methods used to

investigate the performance of the existing SCOT electronics are limited in their accuracy for a number of reasons. Measurements made for both the amplification gain investigation and the current output investigation were discreet data points read off an oscilloscope or multimeter at inconsistent frequencies. A more thorough investigation would require more accurate measurement of these quantities using a data acquisition system.

Appendix C Method for Soldering Magnet Wires to Probe Elements

The following appendix provides a step by step guide to soldering the magnet wires to the SS ball bearings used in the construction of the new SCOT.

C.1 Positioning the Magnet Wire

Thread the magnet wire through the main central hole of the ball bearing and out the exit hole. Slide the ball bearing over a piece of heat shrink to hold it while soldering.

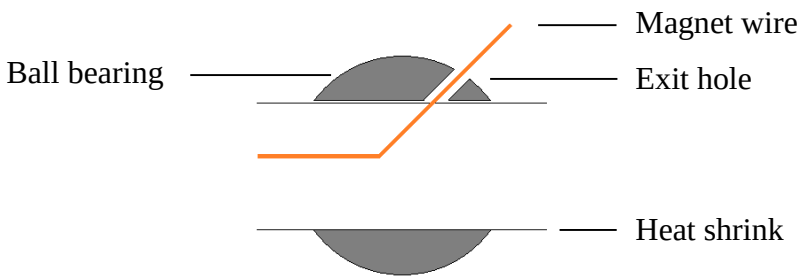

C.2 Positioning the Solder

Use tweezers to place a 4 mm-5 mm length of solder into the exit hole alongside the magnet wire.

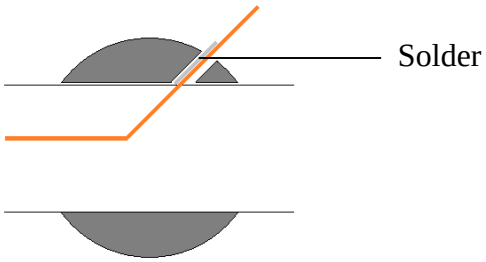

C.3 Soldering the Connection

Apply heat to the underside of the ball bearing opposite the solder until it melts, filling the exit hole.

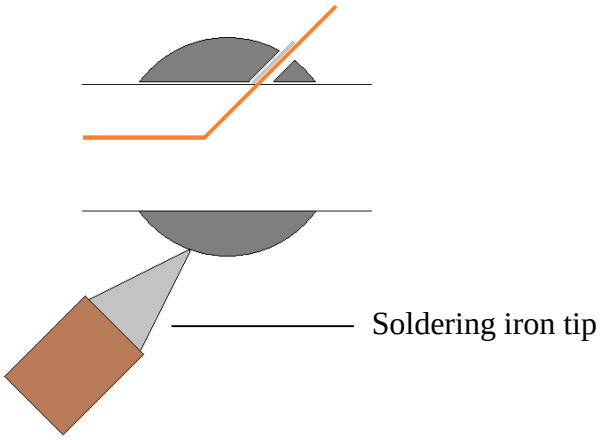

C.4 Clean the Connection

File back the excess solder and remove the excess magnet wire from the connection.

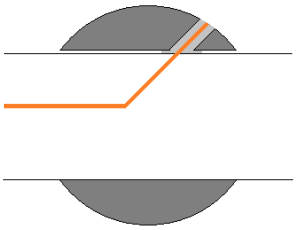

Appendix D High Speed Mechanical Testing of SCOT v6

D.1 Introduction

The original intent of this work was to investigate the signal response and material behavior of the SCOT when subjected to higher loading rates. Data alignment between the SCOT output and the electromagnetic linear actuator data was inhibited due to the data sets' collection on separate DAQ systems. Attempts were made to use a grounding silver foil manual trigger; however, this quick solution was found to work inconsistently during pilots at higher speeds. Instead, the loading of the SCOT sensor undertaken in this study was used to assess the durability of the new SCOT when subjected to faster load rates.

D.2 Methods

The load protocol followed the protocols outlined in Chapters 2 and 3. The SCOT sensor was subject to loading at target displacement rates of 500 mm/s, 1000 mm/s and 2000 mm/s to a target displacement of 8 mm using an electromagnetic linear actuator (TestBench ELF LM-1, Bose Corporation, Eden Prairie, MN). The sensor was loaded three times at each load rate. After testing at each load rate, a qualitative assessment of the SCOT sensor was performed to see if it still worked by applying finger pressure loading to the SCOT casing.

D.3 Results

An example displacement trace from the trials conducted is presented in Figure D-1. After all loading was complete, the SCOT continued to function, producing a steady unloaded output signal across all SCOT segments.

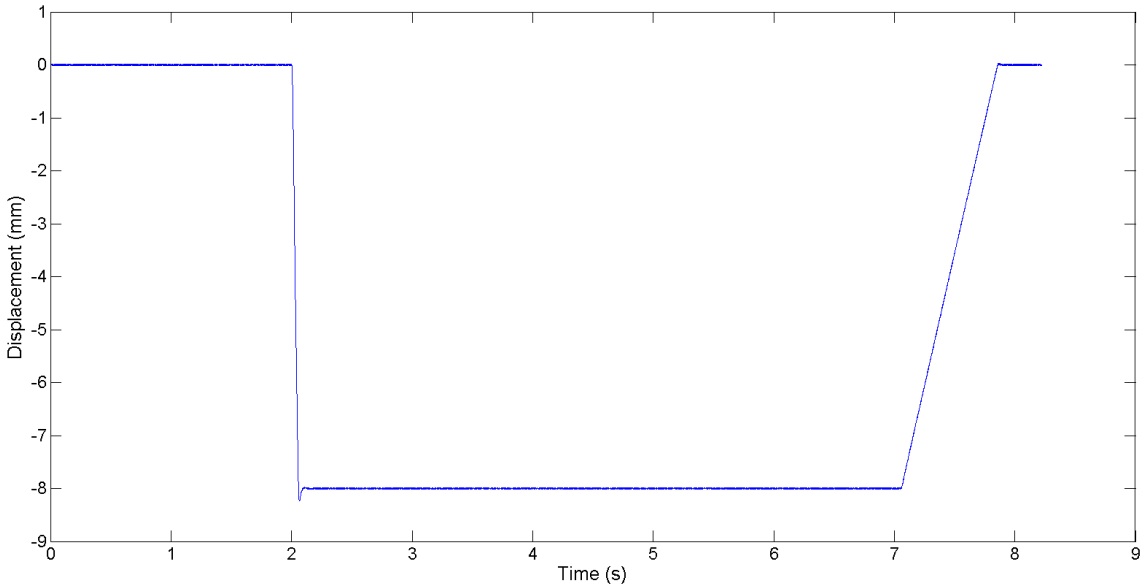

Figure D-1 Example displacement versus time trace from testing of the new SCOT using increased load rates.

D.4 Discussion

The new SCOT continued to function effectively with stable unloaded outputs despite repeated loading at high displacement rates. Since only three trials were performed for each load rate, long term durability of the new design remains in question; however, these tests have subjected the SCOT probe to displacement rates in excess of those it will be subjected to in future studies (500 mm/s).

A more detailed study of the signal response of the SCOT at load rates up to 500 mm/s (the rates at which future experiments will be conducted) is warranted and should be undertaken if at all possible.

Appendix E ROM Measurements made with Spine Machine Encoder

This appendix has been adapted from a report written by Kenneth Martens completed as part of his Co-Op program

E.1 Objectives

- Verify the motion data produced by the spine machine's optical encoder using the Optotrak system
- Define the accuracy of the spine machine and operating limits where the accuracy declines
- Show that the Optotrak system can collect position data generated as analog signals by the spine machine and cross check those values with the values saved by the spine machine
- Compare the key results found at multiple speeds and torque limits for the two systems (LabVIEW vs. First Principles) for peak angular displacement

E.2 Methods

We attached Optotrak markers to the spine machines in two locations: directly onto the shaft leaving the gearbox, and onto a face on the sample that moves rigidly with the arm (referred to as the "cheese face" because of the block's similar appearance to Swiss cheese).

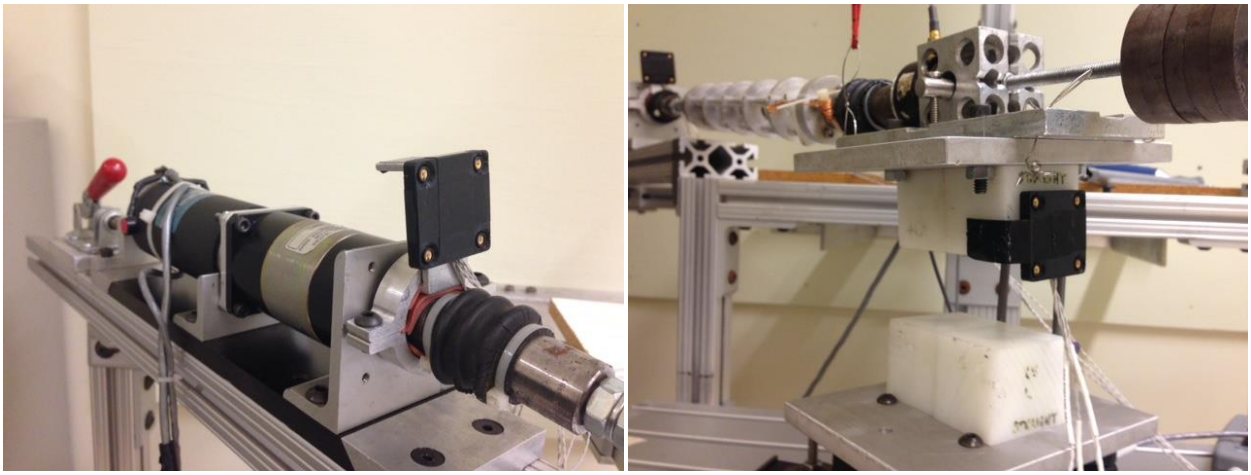

Figure E-1 Marker attached to shaft on gearbox (left), marker attached rigidly to end of arm on test sample (right). Cheese block is mounted to top surface of test sample.

The analog torque signal was wired from the signal conditioner connection in the UMI to a BNC input on the Optotrak ODAU. The analog position signal was generated by the motion controller and wired from the UMI to the ODAU. Finally, a trigger was set up consisting of an open connection wired into an analog input in both the UMI and ODAU. The connection was closed during operation, and the data were aligned based on the first low signal of the trigger input. Operating details for each trial are outlined in Table D1 below.

Table E-1 Details of the trials run on the spine machine for verification. Trials 11-14 are omitted because errors occurred during data collection

Trial	Orientation	Material	Velocity (deg/s)	Torque (Nm)
1	Horizontal	PEEK	1.5	2.5
2	Horizontal	PEEK	2.5	2.5
3	Horizontal	PEEK	2.5	3.5
4	Horizontal	PEEK	1.5	3.5
5	Vertical	PEEK	1.5	1.5
6	Vertical	PEEK	1.5	2.5
7	Vertical	PEEK	2.5	2.5
8	Vertical	PEEK	2.5	3.5
9	Vertical	PEEK	2.5	5
10	Vertical	PEEK	2.5	7.5
15	Horizontal	Titanium	1	10

For each trial, the Optotrak and spine machine data were analyzed in MATLAB. A reference coordinate system was created from digitized points from the stationary base and motor block face and all the Optotrak motion was calculated relative to that coordinate system. Kinematics code adapted from Angela Melnyk's code for the lateral bending project was used. Angela's code was adapted from code from Robyn Newell.

In brief, the analysis in MATLAB:

- The program loads the following data:
    - marker data from the Optotrak file, the spine machine encoder motion from the ODAU file, and spine machine encoder motion from the TDMS spine machine file
    - torque data from the ODAU file and the TDMS spine machine file
    - trigger data from the ODAU file and TDMS spine machine file
    - other operating parameters from the TDMS spine machine file
- Pads the TDMS file to align the data based on the offset measured from the trigger
- Calculates the values and locations of the peak positions and torques and compares the different values to the values recorded in the TDMS file
- Creates and saves figures and data tables with the above calculations

E.3 Results and Observations

As expected, the ODAU and TDMS position data matches very well. These signals are both representations of the spine machine encoder. The motion captured by the Optotrak markers on the motor output is similar to the encoder, but they tend to have a slightly lower magnitude. The motion of the cheese face, or test sample, always shows less motion than the encoder. This is due to backlash in the U-joints and out of plane motion. Both of those phenomena are visible on the position plots (Figure D2). When comparing multiple trials, I observed that the cheese ace markers differ from the expected value more when the specimen is stiffer, the applied torque is higher, and when the orientation is vertical instead of horizontal.

NOTE: The differences caused by orientation are likely due to the ways the sample rods I tested bend in the different orientations and not inherently in the orientation itself.

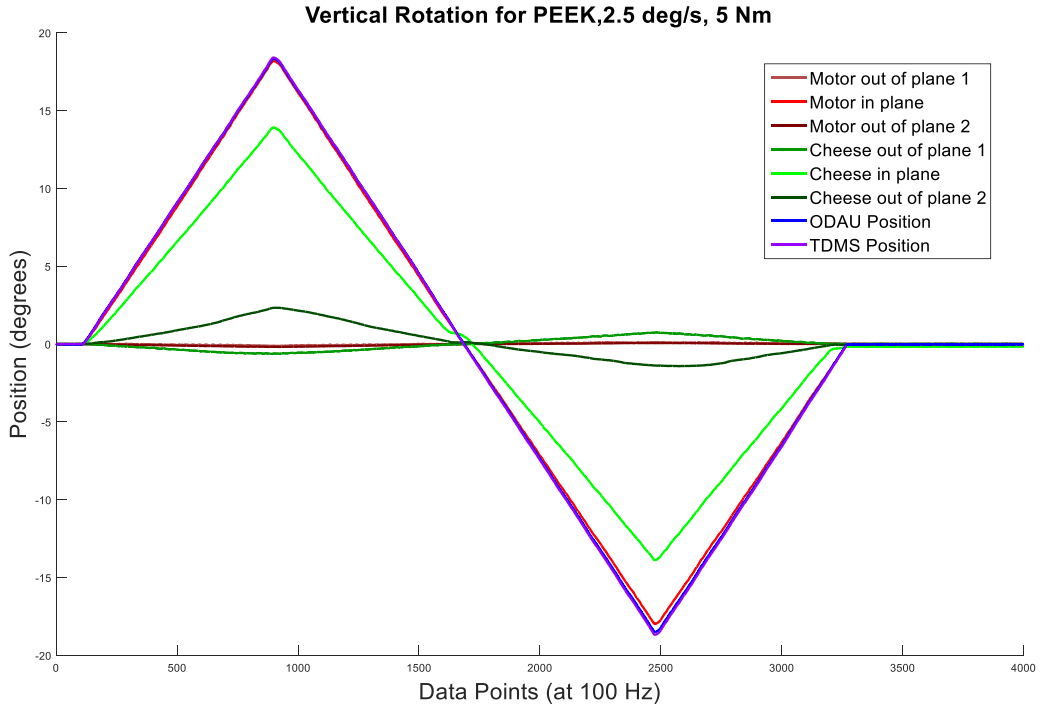

Figure E-2 The cheese face motion is less than the encoder motion and it has larger motions in the out of plane axes. The encoder motion captured by the TDMS and ODAU systems are similar and expected.

Table E-2 Summary of position data: The "delta" columns show the difference from each data sources position value to the TDMS position value for both maximum and minimum position. The "percent" columns show the percent that the "delta" is of that TDMS value.

Row	Motor max delta	Motor min delta	Motor max percent	Motor min percent	Cheese max delta	Cheese min delta	Cheese max percent	Cheese min percent	ODAU max delta	ODAU min delta	ODAU max percent	ODAU min percent
Test001	-0.192	0.187	-1.319	-1.484	-2.963	1.794	-20.355	-14.233	0.024	0.151	0.168	-1.195
Test002	-0.193	0.182	-1.315	-1.453	-2.964	1.772	-20.215	-14.127	-0.020	0.093	-0.134	-0.738
Test003	-0.205	0.278	-0.996	-1.556	-3.741	2.387	-18.147	-13.340	-0.013	0.186	-0.064	-1.041
Test004	-0.206	0.279	-0.993	-1.568	-3.736	2.428	-18.030	-13.642	-0.029	0.169	-0.138	-0.952
Test005	-0.193	0.245	-3.579	-4.010	-1.608	2.204	-29.877	-36.094	0.090	0.099	1.677	-1.618
Test006	-0.270	0.348	-3.030	-3.682	-2.460	2.878	-27.610	-30.480	0.121	0.176	1.358	-1.867
Test007	-0.285	0.340	-3.170	-3.600	-2.466	2.904	-27.407	-30.773	0.032	0.105	0.360	-1.115
Test008	-0.208	0.523	-1.642	-4.048	-3.364	3.541	-26.564	-27.396	-0.030	0.087	-0.234	-0.672
Test009	-0.199	0.697	-1.083	-3.732	-4.492	4.780	-24.403	-25.585	-0.037	0.154	-0.200	-0.823
Test010	-0.163	0.868	-0.547	-2.894	-7.081	7.319	-23.822	-24.406	-0.057	0.288	-0.193	-0.959
Test015	-0.262	0.000	-1.356	0.000	-10.750	0.000	-55.673	0.000	-0.145	0.000	-0.750	0.000
Average	-0.216	0.395	-1.730	-2.803	-4.148	3.201	-26.555	-23.008	-0.006	0.151	0.168	-1.098

Motion at the end of the arm is not the same as what the spine machine records. This is due to backlash in the U-joints and rotation that occurs out-of-plane. The backlash is evident by the 'step' in the cheese face position plot and the out-of-plane motion is visible on position plots for the two out-of-plane axes. This results in both positions and velocities at the end of the arm that are less than that of the motor and thus the TDMS data. For this reason, it is necessary to use Optotrak markers with any specimen tested in the machine when the position of the specimen must be tracked.